

# Strings of diquark-quark (QQ)Q baryon before phase transition

---

**A. S. Bakry**

*Institute of Modern Physics, Chinese Academy of Sciences, Gansu 730000, China*  
*E-mail: ahmed.bakry@mail.com*

**M. A. Deliyergiyev**

*Department of Nuclear Particle Physics, University of Geneva, CH-1211, Switzerland*  
*E-mail: maksym.deliyergiyev@outlook.com*

**A. A. Galal**

*Department of Physics, Al Azhar University, Cairo 11651, Egypt*

**M. N. Khalil**

*Department of Mathematics, Bergische Universität Wuppertal, 42097 Germany*  
*Department of Physics, University of Ferrara, Ferrara 44121, Italy*  
*Computation-based Science Research Center, Cyprus Institute, Nicosia 2121, Cyprus.*  
*Department of Physics, Al Azhar University, Cairo 11651, Egypt*

**A. M. Khalaf**

*Department of Physics, Al Azhar University, Cairo 11651, Egypt*

ABSTRACT: We explore the limit at which the effective baryonic Y-string model of the junction approaches the mesonic stringlike behavior. We calculate and compare the numerical values of the static potential and energy-density correlators of diquark-quark and quark-antiquark configurations. The gauge model is pure Yang-Mills  $SU(3)$  lattice gauge theory at coupling  $\beta = 6.0$  and finite temperature. The diquark setup is approximated as two quarks confined within a sphere of radius 0.1 fm. The lattice data of the potential and energy show that the string binding the diquark-quark configuration displays an identical behavior to the quark-antiquark confining string. However, with the temperature increase to a small enough neighborhood of the critical point  $T_c$ , the gluonic symmetries between the two systems do not manifest neither at short nor intermediate distance scales. The comparison between the Polyakov loop correlators and the second moment of the action-density correlators for both systems shows significant splitting. This suggests that subsisted baryonic decoupled states overlap with the mesonic spectrum. The baryonic junction's model for the potential and the profile returns a good fit to the numerical lattice data of the diquark-quark arrangement. However, near the critical point, the mesonic string displays large deviations compared to fits of the corresponding quark-antiquark data.

KEYWORDS: QCD Phenomenology, Lattice Gauge Theory, finite-temperature, bosonic strings, baryonic strings, flux tubes, Nambu-Goto theory, effective actions, Polyakov-Kleinert.

---

## Contents

<b>1. Introduction</b>	<b>1</b>
<b>2. Hadronic string phenomenology</b>	<b>3</b>
2.1 Mesonic string potential	4
2.2 Baryonic Y-string potential	6
2.3 Mesonic String Width	10
2.4 Baryonic String Width	11
<b>3. Lattice measurements</b>	<b>13</b>
3.1 Potential operators	13
3.2 Energy-density operators	14
3.3 Lattice parameters and Monte-Carlo updates	15
3.4 Cooling method	17
<b>4. Diquark-quark (QQ)Q potential</b>	<b>20</b>
<b>5. Diquark-quark (QQ)Q energy profile</b>	<b>27</b>
5.1 Vacuum's Action-density	27
5.2 Broadening of effective strings	37
<b>6. Conclusion and prospect</b>	<b>42</b>
<b>A. Appendix A</b>	<b>43</b>

---

## 1. Introduction

Baryons are viewed as the bound states of the three quarks in the conventional quark model, with two relative coordinates as manifestations of the internal space-time degrees of freedom. In the quark-diquark model, two of the three quarks are bound together to create a boson (diquark) system, with the third quark assumed to revolve around this boson.

The concept of a diquark is long-established as the quark model itself. Gell-Mann introduced the notion of the diquark in [1], and shortly afterward constituent quark-diquark models for baryons were constructed by Ida and Kobayashi [2] and Lichtenberg et al. [3–5] also explores the electromagnetic characteristics of the baryons within the model's framework.

The diquark model was provoked later to describe several strong interaction phenomena [6–13]. In the recent past, there has been reviving interest in the characteristics of diquarks in hadronic systems, since they may debut a key role in the formation of exotic states.

The pertinence between strings and gauge field theory [14] of hadrons is a long-standing conjecture [15, 16]. The Nambu-Nielsen-Susskind-Goto string [17] with point masses at its ends is produced by the interaction of two oppositely (magnetically) charged monopoles with a massive gauge field (mass  $\mu$ ) in the limit  $\mu \rightarrow \infty$  [18]. Another finding is that a non-abelian gauge theory's limit would resemble the dual string model [19].

It may thus be presumed that a meson can be thought of as two point-quarks bound together by a string, and a baryon as three point-quarks joined up by three strings. Representing the point quarks as Dirac fields constrained to world lines allows for the assignment of appropriate internal quantum numbers [20, 21]. The startling outcome of this approach is that the QCD equivalent of the string model theory of hadron dynamics [22].

Now, we have theoretical developments related to hadronic string models on both the mesonic and baryonic configurations [23–28]. These studies have investigated the mass of diquarks [29–33], and, more recently, the nature of diquark correlations [34].

In  $SU(3)$  color group, a diquark, two quarks in close vicinity to each other, transform according to the conjugate representation  $[\bar{3}]$ . The scalar-diquark channel is attractive in the spin-singlet rather than the spin-triplet of the axial vector diquark. Hence low-lying diquarks lie within the conjugate representation  $[\bar{3}]$  and acquire (+) parity and belong to the color  $[\bar{3}]$ , and thereof, share common properties to the antiquark.

Owing to the formation of flux tubes of the same energy density and transverse size, the long-range confining force put forth to the linearly rising slope of the quark-antiquark potential [35–37]. The target of this investigation is to scrutinize this interesting limit in lattice QCD if the quark-diquark flux tubes [38–53] at high temperatures with similar physical characteristics.

In a previous report, we show that the hadronic Y-string systems in static baryonic forms on the lattice at finite temperatures  $T$  when adopting Polyakov loops [54] as quark operators [38–40]. Within this investigation, base lengths as or larger than  $A = 0.6$  fm for isosceles triangle three-quark configurations were analyzed. Three Gaussian-like flux tubes were observed to emerge in the form of a Y-shape string.

However, the investigation of the properties of the quark-antiquark ( $Q\bar{Q}$ ) versus the properties of the diquark-quark ( $(QQ)Q$ ) configurations effective bosonic strings has not fully addressed on the lattice and in extreme conditions such as high temperature [55, 56] in particular.

In this paper, we expand our investigation of three-quark systems to the scenario in which two quarks interact to create a closely bound state or a diquark [38–40] which then engages in interaction with a third quark to create a baryon.

The paper is organized as follows: We review the free bosonic string theory for the baryon and meson in Sec. 2. The simulations setup and lattice measurement operators will be described in Sec. 3. In Sec. 4 we measure and compare the numerical data of the potential of the  $Q\bar{Q}$  and the  $(QQ)Q$  systems. The string model implications for each of these systems are discussed and compared with the numerical data at a variety of quark configurations.

We present the action density analysis of both the  $Q\bar{Q}$  and the  $(QQ)Q$  systems in Sec. 5. The baryonic profile of the junction and meson strings and the broadening aspects of the Monte-Carlo data are scrutinized at several transverse planes. In the last section, Sec. 6 concluding remarks are drawn.

## 2. Hadronic string phenomenology

It has long been hypothesized that in a pure Yang-Mills (YM) vacuum, a stable string-like structure can develop, which binds static color charges and results in linearly growing potential. Through the dual Meissner effect, the QCD vacuum confines the color fields into a string that is dual to the Abrikosov line in the dual superconductor model of the QCD vacuum [57, 58]

Further, It was suggested to employ an idealized system of bosonic strings to describe flux tubes transmitting the strong interaction between the color sources [16, 59]. The formation of stringlike topological defects is not exceptional to QCD [14, 60–73], and arises in numerous strongly interacting systems such as vortices in superfluids [74], flux tubes in superconductors [75], vortices in Bose-Einstein condensates [76], Nielsen-Olesen vortices of field theory [77], and cosmic strings [78]. The physical parameters pertinent to each strongly interacting system are what determine this object’s characteristics. Certain phases of the model do, however, exhibit quantifiable impacts of quantum fluctuations.

The classical solution breaks the translational invariance of the (YM) vacuum in a mesonic string picture [79–84], resulting in the creation of massless Goldstone modes [86]. In the so-called rough phase of lattice gauge theories, the quantum fluctuations cause the linearly rising potential to experience the Lüscher subleading correction on distance scales greater than the intrinsic thickness of the flux tube  $1/T_c$  [87].

As the theory’s coupling drops, the roughening transition occurs, and the flux tube admits a collective coordinate description that lays out a logarithmic rise in the fluctuations’ mean-square width with the length of the string [90].

This is been confirmed by accurate lattice measurements of the potential for color source separation starting at a distance of  $R = 0.4$  fm [59]. Investigation of other confining gauge models has also confirmed these predictions [87–89, 91].

The Y-ansatz, which represents the leading string effect, can adequately characterize the long-distance lattice data of the confining potential at zero temperature [26, 27]. The Y potential the two loop perturbative calculations and strong coupling approximation as well [92–97].

Suchlike the mesonic string, the impact of quantum fluctuations of the Y-string on the  $3Q$  potential have been reported [26]. The calculations of the Casimir energy in this model have indicated a geometrical Lüscher-like a next to leading term to the Y-( $3Q$ ) potential [27]. The Lüscher-like term is a gauge group-independent and depends only on the geometry of the three static color charges.

At sufficiently high temperatures, the equations of motion of a Nambu-Goto type bosonic string for the width of the action density at the middle plane between two quarks predict a linear broadening in the tube’s diameter [98]. At high temperatures, the inclusion

of higher-order string's self-interactions and other effects [91, 99–114] improves the match between the lattice data and the mesonic string model [115–122]. That is, we expect no peculiarities thereabout the hypothesis that the vibration of this underpinning Y-shaped string system is the source of the observed gluonic distribution at high temperature.

The string model assumptions of the effective description of the tube with a collective coordinate referring to the underlying thin-string are working at high temperature [53]. This is of particular relevance when discussing a Y-shaped baryonic string model [26–28] to scrutinize the large distance  $\Delta$  baryonic flux arrangement [52, 123].

The foregoing main points mount the rationale for discussing the lattice gauge theory data versus string models at color charge separation temperature when a crossover from the junction behavior to the free mesonic string model could come about.

## 2.1 Mesonic string potential

Physical IR features of the string's world sheet ought to compare to with what is predicted for a QCD flux tube. The dynamics of the flux tube follow a massless and free-string theory in the IR limit; given large enough color source separation, an effective field theory with infrared action may be described as

$$\begin{aligned} S[\mathbf{X}] &= S_{cl} + S_0[\mathbf{X}] \\ &= \sigma R L_T + \frac{1}{2} \int d\zeta_0 \int d\zeta \left( \frac{\partial \mathbf{X}}{\partial \zeta_\alpha} \cdot \frac{\partial \mathbf{X}}{\partial \zeta_\alpha} \right), \end{aligned} \quad (2.1)$$

where  $S_{cl}$  is the classical configuration or perimeter-area term, the coordinates  $\zeta_0$  and  $\zeta$  parameterize the world sheet ( $\alpha = 0, 1$ ), the vector  $X^\mu(\zeta_0, \zeta)$  in the transverse gauge describes the fluctuations of the two-dimensional bosonic world sheet relative to the surface of minimal-area/the classical configuration with ( $\mu = 1, 2, \dots, d - 2$ ) and the action  $S_0[\mathbf{X}]$  is known as the Gaussian term. The above action  $S[\mathbf{X}]$ , Eq.(2.1), is referred to as the free bosonic string action.

The free bosonic string theory can be obtained from the truncated perturbative expansion of the NG string action. The NG string action is the simplest possible action that is proportional to the world sheet area

$$S^{\text{NG}} = \frac{1}{2} \int d^2\zeta \sqrt{g} g^{\alpha\beta} \frac{\partial \mathbf{X}}{\partial \zeta_\alpha} \cdot \frac{\partial \mathbf{X}}{\partial \zeta_\beta}, \quad (2.2)$$

where  $g^{\alpha\beta}$  is the intrinsic metric induced on the two-dimensional world sheet and parametrized by  $X_\mu(\zeta)$  embedded in the background  $R^D$

$$g^{\alpha\beta} = \frac{\partial \mathbf{X}}{\partial \zeta_\alpha} \cdot \frac{\partial \mathbf{X}}{\partial \zeta_\beta}, \quad (\alpha, \beta = 1, 2, \dots, D - 2), \quad g = \det(g^{\alpha\beta}). \quad (2.3)$$

The Dirichlet boundary condition, corresponding to fixed displacement vector at the ends  $\zeta = 0$  and  $\zeta = R$ , and periodic boundary condition in time  $\zeta_0$  with period  $L_T = 1/T$ , proportional to the inverse temperature scale. For string tension  $\sigma$  and classical area of an

open-string world sheet given by  $A = L_T R$  the NG action  $S^{\text{NG}}$  can be expanded [124] in a natural dimensionless parameter  $(\frac{1}{\sigma A})$  such that

$$\begin{aligned}
S^{\text{NG}}[\mathbf{X}] &= S_{\text{cl}} + S_0[\mathbf{X}] + S_1[\mathbf{X}] + \dots \\
&= S_{\text{cl}} + S_0[\mathbf{X}] \\
&+ \frac{1}{\sigma A} \int \int d\zeta_0 d\zeta \left[ \left( \frac{\partial \mathbf{X}}{\partial \zeta_\alpha} \cdot \frac{\partial \mathbf{X}}{\partial \zeta_\alpha} \right)^2 + \left( \frac{\partial \mathbf{X}}{\partial \zeta_\alpha} \cdot \frac{\partial \mathbf{X}}{\partial \zeta_\beta} \right)^2 \right] \\
&+ \mathcal{O}\left(\frac{1}{(\sigma A)^2}\right).
\end{aligned} \tag{2.4}$$

With truncation that holds in the long string limit, the aforementioned expression is the effective string action at low energy. Changing from the physical units [125] of the bosonic fields to dimensionless form  $\frac{\mathbf{X}}{\sqrt{\sigma}} \rightarrow \mathbf{X}$ , the leading-order (LO) and the NLO terms of NG action after field redefinition can be written as

$$\begin{aligned}
S_{\text{lo}}^{\text{NG}}[\mathbf{X}] &= \sigma R L_T + \frac{\sigma}{2} \int d\zeta_0 \int d\zeta \left( \frac{\partial \mathbf{X}}{\partial \zeta_\alpha} \cdot \frac{\partial \mathbf{X}}{\partial \zeta_\alpha} \right), \\
S_{\text{nlo}}^{\text{NG}}[\mathbf{X}] &= \sigma \int d\zeta_0 \int d\zeta \left[ \left( \frac{\partial \mathbf{X}}{\partial \zeta_\alpha} \cdot \frac{\partial \mathbf{X}}{\partial \zeta_\alpha} \right)^2 + \left( \frac{\partial \mathbf{X}}{\partial \zeta_\alpha} \cdot \frac{\partial \mathbf{X}}{\partial \zeta_\beta} \right)^2 \right].
\end{aligned} \tag{2.5}$$

The Casimir energy is extracted from the string partition function as

$$V(R, T) = -\frac{1}{L_T} \log [Z(R, T)]. \tag{2.6}$$

The partition function of the free NG model in the physical gauge is a functional integral over all the world sheet configurations swept by the non-interacting string

$$Z(R, T) = \int_{\mathcal{C}} [D\mathbf{X}] \exp(-S(\mathbf{X})). \tag{2.7}$$

For a periodic boundary condition along the time direction such that

$$X(\zeta_0 = 0, \zeta_1) = X(\zeta_0 = L_T, \zeta_1), \tag{2.8}$$

with an extent equals to the inverse of the temperature  $L_T = \frac{1}{T}$  and Dirichlet boundary condition at the sources position given by

$$X(\zeta_0, \zeta_1 = 0) = X(\zeta_0, \zeta_1 = R) = 0. \tag{2.9}$$

The path integral Eq.(2.7) and Eq.(2.6) yields the static potential for the leading order contribution Eq.(2.5) of the NG action  $S_{\text{lo}}^{\text{NG}}$ . The eigenfunctions are given by

$$\phi_{mn} = e^{2\pi i \left( \frac{m}{R} + \frac{n}{L_T} \right)}, \tag{2.10}$$

and eigenvalues of  $-\Delta$  are given by

$$\Gamma_{nm} = \left( \frac{2\pi n}{L_T} \right)^2 + \left( \frac{2\pi m}{R} \right)^2. \tag{2.11}$$

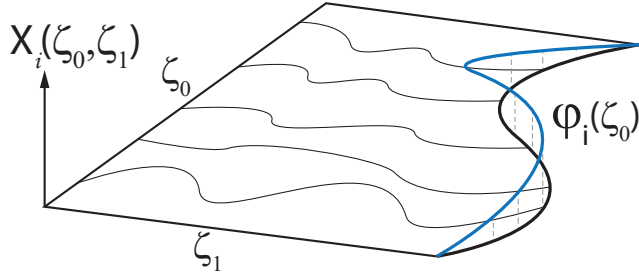


**Figure 1:** World sheet traced by one of the strings up to the junction position.

The determinant of the Laplacian after  $\zeta$  function regularization [101] reads

$$\det(-\Delta) = \left( q_1^{\frac{1}{24}} \prod_{n=1}^{\infty} (1 - q_1^n) \right)^2, \quad (2.12)$$

where  $q = e^{-2\pi\tau}$  and  $\tau = \frac{LT}{2R}$  is the modular parameter of the cylinder. The partition function and the static potential are given by

$$Z_{\ell_0}^{\text{NG}} = e^{-\sigma RT - \mu(T)} [\det(-\Delta)]^{-\frac{(d-2)}{2}}, \quad (2.13)$$

$$V_{\ell_0}^{\text{NG}}(R, T) = \sigma_0 R + (d-2)T \log \eta(\tau) + \mu T, \quad (2.14)$$

$\mu$  is a UV-cutoff and  $\eta$  is the Dedekind  $\eta$  function defined on the real axis as

$$\eta(\tau) = q_1^{\frac{1}{24}} \prod_{n=1}^{\infty} (1 - q_1^n). \quad (2.15)$$

The Lüscher term for the interquark potential is provided by the second term on the right. This term refers to a universal quantum effect that characterizes the CFT in the infrared free-string limit and which is independent of the interaction terms of the corresponding effective theory. The slope of the linear terms in  $R$  can be used to determine how string tension varies with temperature.

Considering the modular transform of the Eq.(2.14)  $\tau \rightarrow 1/\tau$  and taking the limit of a long string, the renormalized string tension [126, 127] to leading order is given by

$$\sigma(T) = \sigma_0 - \frac{\pi(d-2)}{6} T^2 + \mathcal{O}(T^4). \quad (2.16)$$

## 2.2 Baryonic Y-string potential

In the Y-string model [26, 28, 128, 129] the quarks are connected by three strings that come together at a junction [130–135]. The string world sheets' smallest area corresponds to the classical arrangement. The world sheet (blade) of each string is made up of a static quark line and a fluctuating junction world-line (Fig. 1 and Fig. 2). The parameter  $\zeta_1$  and  $\zeta_0$  (time) label the position on string world-sheet (blade)  $i$ . The position of the junction is given by  $\zeta_1 = L_i + \eta_i \cdot \phi(\zeta_0)$ . The transverse fluctuations  $X_i(\zeta_0, \zeta_1)$  vanish at the location

of the quarks ( $\zeta_1 = 0$ ), and are periodic in the time  $\zeta_0$ , with period  $1/L_T$  (see Fig. 1) and is the temporal extent governing the inverse temperature.

That is, the Dirichlet boundary condition in addition to the boundary condition from continuity of the transverse fluctuations  $X_i(\zeta_0, \zeta_1)$

$$X_i(\zeta_0, L_i + \eta_i \cdot \phi(\zeta_0)) = \phi_{\perp i}(\zeta_0), \quad (2.17)$$

where  $\eta_i$  are spatial unit vectors in the direction of the strings such that  $\sum_i \eta_i = 0$ . The NG action after gauge-fixing and expanding around the equilibrium configuration yields

$$S_{\text{Fluct}} = \sigma L_Y L_T + \frac{\sigma}{2} \sum_{i,j} \int_{\Theta_i} d^2\zeta \frac{\partial \xi_i}{\partial \zeta_j} \cdot \frac{\partial X_i}{\partial \zeta_j}, \quad (2.18)$$

where,  $L_Y = \sum_i L_i$  above denotes the total string length. In this model [26, 28], the junction is assumed to acquire a self-energy term  $m$ . This results in an additional boundary term to NG action

$$S = S_{\text{Fluct}} + S_{\text{Boundary}},$$

with a static energy and a kinetic energy terms of junction defined as

$$S_{\text{Boundary}} = \left( mL_T + \frac{m}{2} \int_0^{L_T} dt |\dot{\phi}|^2 \right),$$

respectively.

The system's partition function is

$$Z = e^{-(\sigma L_Y + m)L_T} \int D\phi \exp\left(-\frac{m}{2} \int dt |\dot{\phi}|^2\right) \prod_{i=1}^3 Z_i(\phi), \quad (2.19)$$

where  $Z_i(\phi)$  denotes the  $i$ -th partition function of a given blade which bounded by the junction worldline  $\phi(t)$ :

$$Z_i(\phi) = \int_{\phi} DX_i \exp\left(-\frac{\sigma}{2} \int |\partial X_i|^2\right). \quad (2.20)$$

The Nambu-Goto type string action combined with a Dirichlet boundary condition at the static color sources can be utilized to characterize the Y-string. In this approach, the action, in addition to a boundary term that takes junction fluctuations into account, is proportional to the entire area of the three blade world sheet system swept by the fluctuating world lines of the strings [26]. That is, the Y-string system acquires a mixed Dirichlet-Neumann boundary condition [136]. The string's partition function  $Z_i(\phi)$  in  $D$  dimensions [26] is given by

$$Z_i(\phi) = e^{-\frac{\sigma}{2} \int |\partial X_{\min,i}|^2} |\det(-\Delta_{\Theta_i})|^{-(D-2)/2}, \quad (2.21)$$

where  $X_{\min,i}$  is the minimal-area solution for a given junction configuration  $\phi(\zeta_0)$ , and  $\Delta_{\Theta_i}$  denotes the Laplacian acting on the domain (blade)  $\Theta_i$ .

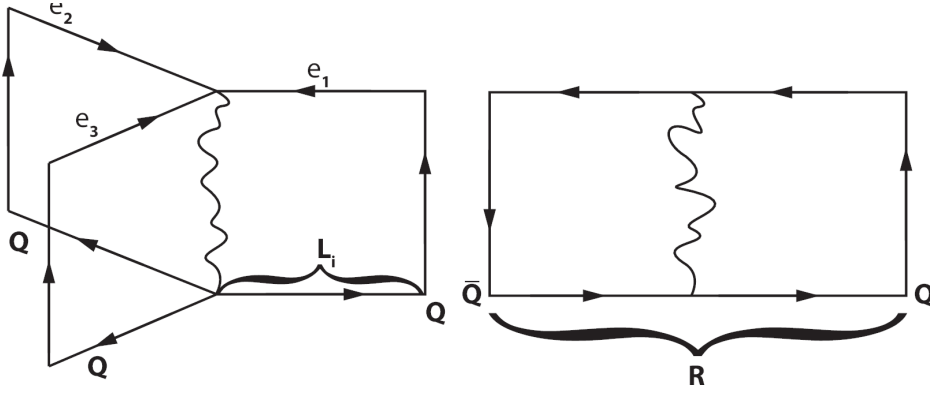


**Figure 2:** The three and two blade worldsheet systems swept by the fluctuating world lines of the gluonic strings of the baryon and meson.

The Casimir energy has been computed for the baryonic potential  $V_{3Q}$  by Jahn and deForcrand [26, 27]. In that approach, the resultant domains were conformally mapped to rectangles before the Laplacian's determinant was evaluated in Eq.(2.21).

The calculation of the corresponding partition function Eq.(2.19) requires evaluating the integral over the minimal area swept due to perpendicular fluctuations  $\phi$ , and the determinant of the Laplacian.

Conformal mapping the string's blade  $a$  to a rectangle [26], see Fig.2

$$f_i(z) = z + \frac{1}{\sqrt{L_T}} \sum_{w \neq 0} \frac{\eta_i \cdot \phi_w}{\sinh(wL_i)} e^{wz}. \quad (2.22)$$

The minimal area solution for a fixed junction configuration

$$X_{\min,i} = \frac{1}{\sqrt{L_T}} \sum_w \phi_{w,zi} \frac{\sinh(ws)}{\sinh(wL_i)} e^{iwt}, \quad (2.23)$$

taking into account that the minimal-area solution for a fixed position of the junction,  $X_{\min,i}(t, s)$ , is harmonic and satisfies the boundary conditions

$$\Delta X_{\min,i} = 0, \quad X_{\min,i}(t, L_i + \eta_i \cdot \phi(t)) = \phi_{zi}(t). \quad (2.24)$$

The integral in Eq.(2.20) would then read

$$\int_{\Theta_i} d^2 \zeta \sum_i \frac{\partial X_{\min,i}}{\partial \zeta_i} \cdot \frac{\partial X_{\min,i}}{\partial \zeta_i} = \sum_w w \coth(wL_i) |\phi_{w,zi}|^2. \quad (2.25)$$

The determinant in Eq.(2.21) is obtained by mapping the domain  $\Theta_i$  conformally to a rectangle  $L'_i \times L_T \equiv \tilde{\Theta}_i$ . Taking into account the change in the Laplacian [28, 59]. Using the above conformal map Eq.(2.22), we obtain to leading order

$$\ln \frac{\det(-\Delta_{\Theta_i})}{\det(-\Delta_{\tilde{\Theta}_i})} = \frac{1}{12\pi} \sum_w w^3 |\eta_i \cdot \phi_w|^2 \coth(wL_i), \quad (2.26)$$

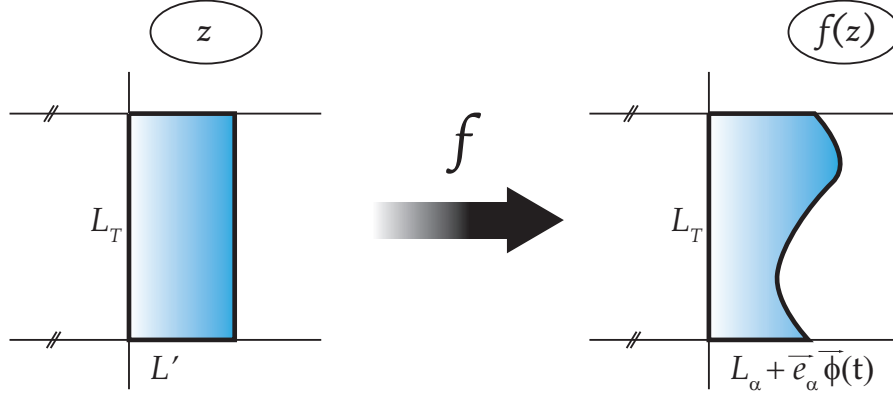


**Figure 3:** Conformal map Eq. (2.22) maps the domain  $\theta_i$  conformally to a rectangle  $L'_i \times L_T \equiv \tilde{\Theta}_i$ .

Further, conformally mapping the above into a circle and making use of Eq. (2.26), the determinant of the Laplacian with respect to the blade  $a$  would then read

$$\det(-\Delta_{\theta_i}) = \eta^2 \left( \frac{iL_T}{2L'_i} \right) \exp \left( -\frac{1}{12\pi} \sum_w w^3 \coth(wL_i) |\eta_i \cdot \phi_w|^2 \right), \quad (2.27)$$

with  $\eta(\tau)$  is the Dedekind function. The sum over all eigenmodes would result in a Lüscher-like correction to the  $V_{3Q}$  potential at zero temperature [26]. The baryonic potential  $V_{3Q}$  then reads

$$V_{3Q}(L_i) = \sigma L_Y + V_{\parallel} + 2V_{\perp} + \mathcal{O}(L_i^{-2}), \quad (2.28)$$

such that  $L_Y \equiv L_1 + L_2 + L_3$  is the minimal of the sum of the lengths of the three strings, and

$$V_{\parallel}(L_i) = \sum_i \frac{1}{L_T} \eta \left( \frac{iL_T}{2L_i} \right) + \sum_{w=0} \frac{1}{L_T} \ln \left[ \frac{1}{3} \sum_{i<j} \coth(wL_i) \coth(wL_j) \right], \quad (2.29)$$

for the in-plane component and

$$V_{\perp}(L_i) = \sum_i \frac{1}{L_T} \eta \left( \frac{iL_T}{2L_i} \right) + \sum_{w=0} \frac{1}{L_T} \ln \left[ \frac{1}{3} \sum_i \coth(wL_i) \right], \quad (2.30)$$

is the potential component due to the perpendicular fluctuations. The corresponding mesonic limit would read

$$V_{\perp} = \frac{1}{L_T} \eta \left( \frac{iL_T}{2L_1} \right) + \frac{1}{L_T} \eta \left( \frac{iL_T}{2L_2} \right) + \sum_{w=0} \frac{1}{L_T} \ln \left[ \frac{1}{2} \coth(wL_1) + \coth(wL_2) \right]. \quad (2.31)$$

The quark-antiquark ( $Q\bar{Q}$ ) potential is then

$$V_{Q\bar{Q}} = \sigma(L_1 + L_2) + \frac{2}{L_T} \ln \left[ \eta \left( \frac{iL_T}{2(L_1 + L_2)} \right) \right], \quad (2.32)$$

which is in agreement with the mesonic string potential (2.14). Expressing the sum in Eq.(2.28) in terms of Dedekind  $\eta$  functions, the potential in the  $3Q$  channel would read

$$V_{3Q} = \sigma L_Y + \frac{\gamma(L_i)}{L_T} \ln \left[ \eta \left( \frac{iL_T}{2L_Y} \right) \right], \quad (2.33)$$

where  $\gamma$  is a geometrical factor depending on the quark configuration (see section(IV)) that can be evaluated numerically from Eq.(2.28).

### 2.3 Mesonic String Width

The string-like object's modes determine the flux tube's physical width. According to an infamous prediction made by Lüscher, Munster, and Weisz [90], which was based on the effective Bosonic string model, the mean square width of the vibrating flux-tube at the centre plane increases logarithmically with the interquark spacing,  $R$ .

$$W^2 \sim \frac{1}{\pi\sigma} \log \left( \frac{R}{\lambda} \right) \quad (2.34)$$

where  $\lambda$  is an ultra-violet scale. With the increase of the temperature, higher-order gluonic excitations come into play and are expected to alter the broadening pattern of the effective width both with the distance and the temperature.

The generic definition of the mean-square width of the string is,

$$\begin{aligned} W^2(\xi; \tau) &= \langle \mathbf{X}^2(\xi; \tau) \rangle \\ &= \frac{\int_{\mathcal{C}} [D\mathbf{X}] \mathbf{X}^2 \exp(-S[\mathbf{X}])}{\int_{\mathcal{C}} [D\mathbf{X}] \exp(-S[\mathbf{X}])}, \end{aligned} \quad (2.35)$$

Assuming  $\zeta = (\zeta_0, i\zeta_1)$  is a complex parametrization of the world sheet, such that  $\zeta_1 \in [-R/2, R/2]$ ,  $\zeta_0 \in [-L_T/2, L_T/2]$ , with redefined as  $\tau = \frac{L_T}{R}$ .

By using the associated Green function, Casselle et al. [87] have calculated the delocalization of the string for all planes that are transverse to the line connecting the quark pair. These calculations are based on first using the Schwinger point-split regularisation [137, 138] to eliminate the divergence in the quadratic operator in Eq.(2.34), and then adopting the corresponding massless free string model.

The quadratic operator is then the correlator of the free bosonic string theory in two dimensions,

$$\begin{aligned} \langle X^2(\zeta_0; \zeta_1) \rangle &= \langle X(\zeta) \cdot X(\zeta + \epsilon) \rangle, \\ &= G(\zeta, \zeta + \epsilon). \end{aligned} \quad (2.36)$$

This Green function is the solution of Laplace equation on cylinder with a Dirichlet boundary condition,

$$G(\zeta, \zeta') = \frac{-1}{2\pi} \log |f(\zeta, \zeta')|. \quad (2.37)$$

The conformal map reads [98],

$$f(\zeta, \zeta') = \frac{\theta_1[\pi(\zeta_1 - \zeta'_1)/R; \tau]}{\theta_2[\pi(\zeta_1 - \zeta'_1)/R; \tau]}, \quad (2.38)$$

where the Jacobi  $\theta$  functions are,

$$\begin{aligned} \theta_1(\zeta_1; \tau) &= 2 \sum_{n=0}^{\infty} (-1)^n q_2^{n(n+1)+\frac{1}{4}} \sin((2n+1)\zeta_1), \\ \theta_2(\zeta_1; \tau) &= 2 \sum_{n=0}^{\infty} q_2^{n(n+1)+\frac{1}{4}} \cos((2n+1)\zeta_1), \end{aligned} \quad (2.39)$$

with the nome,  $q_2 = e^{-2\pi\tau}$ . The expectation value of the mean square width would then read,

$$W^2(\zeta_1) = \frac{1}{\pi\sigma} \log\left(\frac{R}{R_0}\right) + \frac{1}{\pi\sigma} \log\left|\frac{\theta_2(\pi\zeta_1/R)}{\theta'_1(0)}\right|. \quad (2.40)$$

This expression, which converges for modular parameters near unity, also includes a correction term that expresses the dependency of the width at various transverse planes on the modular parameter of the cylinder in addition to the logarithmic divergence term. This term affects the width of all the planes at finite temperatures.

According to the string model, the width will increase as the temperature rises [98, 99, 139–141]. The middle plane experiences the greatest rise in diameter, which is perceived as an increase in the curvature of the string fluctuations' profile. This has been observed [51] as a pronounced effect on the width near the quark positions.

## 2.4 Baryonic String Width

The width of the string at the junction can be calculated [28] taking the expectation value of  $\phi^2$

$$\langle \phi^2 \rangle = \frac{\int [D\phi] \phi^2 e^{-S}}{\int [D\phi] e^{-S}}. \quad (2.41)$$

The above second moment of the junction can be decomposed into perpendicular  $z$  and parallel (in-plane)  $xy$  fluctuations

$$\langle \phi^2 \rangle = \langle \phi_z^2 \rangle + \langle \phi_{xy}^2 \rangle = \frac{I_{z,2}}{I_{z,0}} + \frac{I_{xy,2}}{I_{xy,0}}, \quad (2.42)$$

such that

$$\begin{aligned} I_{z,2} &= \int D\phi_z \phi_z^2 \exp\left\{-\frac{1}{2} \sum_w m w^2 + \sigma w \sum_a \coth(w L_a) |\phi_{w,z}|^2\right\}, \\ I_{xy,2} &= \int D\phi \phi^2 \exp\left\{\sum_w -\frac{1}{2} \left(m w^2 + \sigma w \sum_i \coth(w L_i)\right) |\phi_w|^2 + |\phi_{w,x}|^2 Q_x \right. \\ &\quad \left. + |\phi_{w,y}|^2 Q_y + |\phi_{w,y}|^2 Q_y + 2((\phi_{w,x} \cdot \phi_{w,y})) Q_{xy}\right\}, \end{aligned} \quad (2.43)$$

with  $Q_x$ ,  $Q_y$  and  $Q_{xy}$  defined as in Eq.(2.50). Orthogonalizing the fluctuations for parallel fluctuations the above moments would then read

$$\begin{aligned} I_{x,2} &= \int D\phi_x \phi_x^2 \exp \left\{ \sum_w -\frac{1}{2} (F(w) + G_x(w)) |\phi_{w,x}|^2 \right\}, \\ I_{y,2} &= \int D\phi_y \phi_y^2 \exp \left\{ \sum_w -\frac{1}{2} (F(w) + G_y(w)) |\phi_{w,y}|^2 \right\}, \\ I_{z,2} &= \int D\phi_z \phi_z^2 \exp \left\{ -\frac{1}{2} \sum_w R(w) |\phi_{w,z}|^2 \right\}. \end{aligned} \quad (2.44)$$

$F(w)$ ,  $G(w)$  and  $R(w)$  are defined as

$$\begin{aligned} F(w) &= Q_{x,w} + Q_{y,w}, \\ G(w) &= (Q_{xy,w}^2 + (Q_{x,w} - Q_{y,w})^2)^{1/2}, \\ R(w) &= mw^2 + \sigma w \sum_i \coth(wL_i) \psi(w, L_i). \end{aligned} \quad (2.45)$$

After solving the above Gaussian integrals the components of the width read

$$\begin{aligned} \langle \phi_x^2 \rangle &= \frac{I_{x,2}}{I_{x,0}} = \frac{2}{L_T} \sum_{w>0} \frac{1}{F(w) - G(w)}, \\ \langle \phi_y^2 \rangle &= \frac{I_{y,2}}{I_{y,0}} = \frac{2}{L_T} \sum_{w>0} \frac{1}{F(w) + G(w)}, \\ \langle \phi_z^2 \rangle &= \frac{I_{z,2}}{I_{z,0}} = \frac{2}{L_T} \sum_{w>0} \frac{1}{R(w)}. \end{aligned} \quad (2.46)$$

That is,

$$\langle \phi_z^2 \rangle = \frac{2}{L_T} \sum_{w>0} \frac{1}{mw^2 + \sigma w \sum_i \coth(wL_i) \psi(w, L_i)} \quad (2.47)$$

and the string parallel (in-plane) fluctuations

$$\begin{aligned} \langle \phi_x^2 \rangle &= \frac{2}{L_T} \sum_{w>0} \frac{1}{Q_{x,w} + Q_{y,w} - \sqrt{Q_{xy,w}^2 + (Q_{x,w} - Q_{y,w})^2}}, \\ \langle \phi_y^2 \rangle &= \frac{2}{L_T} \sum_{w>0} \frac{1}{Q_{x,w} + Q_{y,w} + \sqrt{Q_{xy,w}^2 + (Q_{x,w} - Q_{y,w})^2}}, \end{aligned} \quad (2.48)$$

It is more convenient for our further discussion of the in-plane fluctuations on the lattice to consider the above rotated decoupled form, We calculate the string's thickness at the junction position.

Taking into account convoluted fluctuations  $\phi \rightarrow \int_{-\infty}^{\infty} \phi(\tau) \psi(t - \tau) d\tau$  to accelerate the convergence of the series which includes thermal effects. The smoothing  $\psi(w, L_i)$  is given by

$$\psi(w_n, L_i) = \frac{-kw_n}{2\sigma \coth(w_n L_i)} - \frac{2n-1}{4n \coth(w_n L_i)} \left( \frac{2L_i \chi(\tau_i) + 1}{2L_i \chi(\tau_i) - 1} \right)^{2n-1}. \quad (2.49)$$

where  $k$  is an ultraviolet cutoff,  $Q_x, Q_y$  and  $Q_{xy}$  with accordance to [28, 39] are defined as

$$\begin{aligned}
Q_x &= \left( kw^2 + \sigma w \sum_i \coth(wL_i) \psi(w, L_i) \right) + \left( \frac{\sigma}{2} w + \frac{w^3}{12\pi} \right) \left[ \sum_i \eta_{i,x}^2 \coth(wL_i) \psi(w, L_i) \right], \\
Q_y &= \left( kw^2 + \sigma w \sum_i \coth(wL_i) \psi(w, L_i) \right) + \left( \frac{\sigma}{2} w + \frac{w^3}{12\pi} \right) \left[ \sum_i \eta_{i,y}^2 \coth(wL_i) \psi(w, L_i) \right], \\
Q_{xy} &= \left( \frac{\sigma}{2} w + \frac{w^3}{12\pi} \right) \left[ \sum_i \eta_{i,x} \eta_{i,y} \coth(wL_i) \psi(w, L_i) \right].
\end{aligned}
\tag{2.50}$$

### 3. Lattice measurements

#### 3.1 Potential operators

According to QCD at zero temperature, the effective potentials of these two configurations should have the same slope [142] at zero temperature, which would indicate that the flux tubes have the same energy density and transverse size [143, 144]. In this section, we show how to extract the long-range potential and energy density of the  $(Q\bar{Q})$  [126, 145] and  $(QQ)Q$  flux tubes at high temperature.

Rather than the short-distance behavior, which is well represented by the two-body Coulomb-type potential [145, 146], we are interested in pointing out the large-distance IR behavior of the  $3Q$  potential  $V_{3Q}$ , which is directly connected to the characteristics of the confining force.

With a centre symmetry-preserving operator it is possible to calculate the  $3Q$  static potential  $V_{3Q}$  using a transfer matrix interpretation of the Polyakov loops correlator. Within the framework of the Polyakov loop approach, the free energy of a system of three static charges coupled to a heat bath acquires contributions from temperature-dependent changes.

The effective potential is obtained from the Polyakov loops in the standard manner: the static mesonic state is constructed by means of a pair of Polyakov loops

$$\langle \mathcal{P}_{Q\bar{Q}}(\vec{r}_1, \vec{r}_2) \rangle = \langle P(\vec{r}_1) P^\dagger(\vec{r}_2) \rangle
\tag{3.1}$$

where the Polyakov loop on an Euclidean lattice of size  $N_s^3 \times N_t$  is defined as a product of gauge field variables  $U_{\mu=4}(\vec{r}_i, n_t)$ :

$$P(\vec{r}_i) = \frac{1}{3} \text{Tr} \left[ \prod_{n_t=1}^{N_t} U_{\mu=4}(\vec{r}_i, n_t) \right],
\tag{3.2}$$

At fixed temperature  $T$ , assuming the transfer matrix in interpretation is preserved [50], the Monte Carlo evaluation of the temperature-dependent quark-antiquark potential

at each  $R$  is calculated through the Polyakov loop correlators as

$$\begin{aligned}
\langle \mathcal{P}_{Q\bar{Q}}(0, R) \rangle &= \langle P(0)P^\dagger(R) \rangle \\
&= \int d[U] P(0) P^\dagger(R) \exp(-S_w) \\
&= e^{-\frac{1}{T}V_{Q\bar{Q}}(R, T)},
\end{aligned} \tag{3.3}$$

where  $S_w$  is the plaquette action and  $T$  is the physical temperature.

Using Polyakov loop operators, the infinitely heavy quark state is created. For pure  $SU(3)$  gauge setups, the correlators respect the centre symmetry transformation all across the confinement phase.

$$\tilde{U}_{\mu=4}(x, n_t = 1) = C U_{\mu=4}(x, n_t = 1), \tag{3.4}$$

where center  $C$  of the gauge group  $SU(3)$  is all the elements  $z$  such that  $zgz^{-1} = g$ , with  $g \in SU(3)$  or  $z = \exp(2\pi l/3) \in \mathbb{Z}(3)$  with  $l = 0, 1, 2$ . The form of the center symmetry preserving baryonic correlators is then

$$\begin{aligned}
\langle \mathcal{P}_{3Q}(\vec{r}_1, \vec{r}_2, \vec{r}_3) \rangle &\rightarrow \langle \tilde{P}(\vec{r}_1)\tilde{P}(\vec{r}_2)\tilde{P}(\vec{r}_3) \rangle \\
&= \langle e^{2i\pi l} P(\vec{r}_1)P(\vec{r}_2)P(\vec{r}_3) \rangle \\
&= \langle P(\vec{r}_1)P(\vec{r}_2)P(\vec{r}_3) \rangle,
\end{aligned} \tag{3.5}$$

which corresponds to three Polyakov lines all in the same time direction, the vectors  $\vec{r}$  define the positions of the quarks.

The quark-diquark potential can be identified via a three-loop correlator from Eq.(3.5) as

$$\begin{aligned}
\langle \mathcal{P}_{3Q} \rangle &= \langle \tilde{P}(\vec{r}_1)\tilde{P}(\vec{r}_2)\tilde{P}(\vec{r}_3) \rangle \\
&= e^{-\frac{1}{T}V_{3Q}(\vec{r}_1, \vec{r}_2, \vec{r}_3)}.
\end{aligned} \tag{3.6}$$

### 3.2 Energy-density operators

To characterize the Euclidean action density on the lattice we utilize a plaquette operator defined by

$$\square_{\mu\nu}(\vec{\rho}) = 1 - \frac{1}{3} \text{ReTr} \left[ U_\mu(\vec{\rho})U_\nu(\vec{\rho} + \vec{\mu})U_\mu^\dagger(\vec{\rho} + \vec{\nu})U_\nu^\dagger(\vec{\rho}) \right], \tag{3.7}$$

which corresponds to the minimal loop structure on the lattice with the indices  $\mu$  and  $\nu$  corresponding to Lorentz indices. The plaquette operator can be expanded in a power series [147] of the symmetric tensor  $F_{\mu\nu}^c$  such that

$$\square_{\mu\nu}(\vec{\rho}) = 1 - \frac{1}{3} \text{ReTr} \exp \left[ ig a^2 \sum_c F_{\mu\nu}^c(\vec{\rho}) T^c \right], \tag{3.8}$$

where  $g$  is the coupling of Yang-Mills theory, the index  $c$  is color indices and  $T^c$  are the generators of Lie algebra of  $SU(3)_c$ ,

$$S(\vec{\rho}) = \frac{1}{2}(E^2(\vec{\rho}) - B^2(\vec{\rho})). \tag{3.9}$$

The chromoelectric and chromomagnetic components fields are related to the plaquette components at position  $\vec{\rho}$  as

$$E^2(\vec{\rho}) = \sum_i E_i^2(\vec{\rho}) \rightarrow \sum_i \square_{0i}(\vec{\rho}) \quad (3.10)$$

$$B^2(\vec{\rho}) = \sum_i B_i^2(\vec{\rho}) \rightarrow \sum_i \square_{kj}(\vec{\rho}), \quad (3.11)$$

where the index  $i$  of the magnetic field is the complement of the  $jk$ -plaquette component.

A dimensionless scalar field characterizing the Euclidean action density distribution in the Polyakov vacuum, i.e., in the presence of color sources [133] can be defined as

$$\mathcal{C}_{Q\bar{Q}}(\vec{\rho}; \vec{r}_1, \vec{r}_2) = \frac{\langle \mathcal{P}_{2Q}(\vec{r}_1, \vec{r}_2) \rangle \langle S(\vec{\rho}) \rangle - \langle \mathcal{P}_{2Q}(\vec{r}_1, \vec{r}_2) S(\vec{\rho}) \rangle}{\langle \mathcal{P}_{2Q}(\vec{r}_1, \vec{r}_2) \rangle \langle S(\vec{\rho}) \rangle}, \quad (3.12)$$

with the vector  $\vec{\rho}$  referring to the spatial position of the energy probe with respect to some origin, and the bracket  $\langle \dots \rangle$  stands for averaging over gauge configurations and lattice symmetries. Other dimensionful definitions of the correlator (3.12) yield equivalent representation of the width (see, for example Ref. [72]).

The above equation is dimensionless. However, the field densities in physical units [148] would read

$$\sum_c F_{\mu\nu}^c F_{\mu\nu}^c = \frac{2\beta}{a^4} \left[ 1 - \frac{1}{3} \text{Tr}(\square_{\mu\nu}) \right] + \mathcal{O}(a). \quad (3.13)$$

The sum over the color index  $c$  ensures the gauge invariance of the square of the field densities. The measurements are repeated for each time slice and then averaged,

$$S(\vec{\rho}) = \frac{1}{N_t} \sum_{n_t=1}^{N_t} S(\vec{\rho}, t). \quad (3.14)$$

For baryonic systems, a dimensionless scalar field that characterizes the gluonic field can be defined as

$$\mathcal{C}_{3Q}(\vec{\rho}; \vec{r}_1, \vec{r}_2, \vec{r}_3) = \frac{\langle \mathcal{P}_{3Q}(\vec{r}_1, \vec{r}_2, \vec{r}_3) S(\vec{\rho}) \rangle}{\langle \mathcal{P}_{3Q}(\vec{r}_1, \vec{r}_2, \vec{r}_3) \rangle \langle S(\vec{\rho}) \rangle}. \quad (3.15)$$

Due to the cluster decomposition of the operators,  $\mathcal{C}$  should be approaching a value that is  $\mathcal{C} \simeq 1$  away from the interquark space in the quark-diquark state.

### 3.3 Lattice parameters and Monte-Carlo updates

A set of  $SU(3)$  pure gauge configurations is subjected to measurements. For a coupling value of  $\beta = 6.00$ , the configurations are generated using the standard Wilson gauge action[149] on two lattices with a spatial volume of  $36^3$  and temporal extents of  $N_t = 8$  and  $N_t = 10$ . Such temporal lengths correspond to temperatures  $T/T_c = 0.9$  and  $T/T_c = 0.8$ , respectively. The string tension of value,  $\sqrt{\sigma} = 440$  MeV [73, 150, 151] is applied to reproduce the value of the lattice spacing of  $a = 0.1$  fm.

The  $SU(3)$  gluonic gauge configurations have been generated employing a pseudo-heat bath algorithm [152, 153] updating the corresponding three  $SU(2)$  subgroup elements [154]. Each update step consists of one heat bath and 5 micro-canonical reflections.

Following 2000 thermalization update sweeps, the measurements are made. We carry out a series of measurements  $n_{\text{sub}} = 20$  spaced by 70 updates sweeps apart. A total of 500 bins were used for the measurements of the scalar field, Eq.(3.15). We have obtained 10,000 measurements at each temperature for this analysis.

Correlator is evaluated with these sub-measurements binned together. This corresponds to four equations of evaluating Polyakov lines correlators Eq.(3.1) and (3.6) for the meson and baryon with the action-density correlations Eq.(3.12) and (3.15), respectively.

For further noise reduction, we make use of translational invariance as well by computing the correlation on every node of the lattice, averaging the results over the volume of the three-dimensional torus, in addition, to averaging the action measurements taken at each time slice in Eq.(3.14).

As a by-product the simulations on reasonably large lattice sizes would be beneficial to gain high statistics in a gauge-independent manner and also minimize the mirror effects and correlations across the boundaries [73, 155].

The issue of potential cross-correlations among the correlators at varied distances adds another subtlety to the width measurement. The flux-tube operator, Eq. (3.12), and a three-point correlation function made up of two Polyakov loops oriented in opposing directions are used to calculate the field densities. Cross-correlations between measurements made at various distances on the same gauge configuration may be likely to happen in this arrangement when the size of the flux probe operator is unnaturally large.

A well-known technique in LGTs for reducing the discretization errors caused by the lattice spacing is to use nested loops of various length. Large size/extended operators use this technique. To calculate the chromoelectric and chromomagnetic field densities in the current computations, we used the most basic *one-loop field strength tensor operator*, which is proportional to one plaquette and is the smallest loop structure on hypercubic lattices. For the same reason, we refrained employing extended operator-based methods in the stout-link smearing

To the points mentioned above, we may add one more that stems from the lattice configuration, where Monte Carlo simulations with the typical Wilson gauge action guarantee locality [156]. Additionally, the autocorrelation time would diverge as a result of the heat bath and overrelaxation/microcanonical steps [85].

We determine the local string tension and translate it to the lattice spacing  $a$  in Fermi units, using the transfer matrix interpretation [156], in order to verify the regularity of cross-correlation between nearby Polyakov loop correlators.

$$\alpha(\Lambda) e^{-\sigma RL_T} = \langle P(0)P^\dagger(R) \rangle, \quad (3.16)$$

$$\sigma a^2 = -\frac{1}{L_T} \log \left[ \frac{\langle P(0)P^\dagger(R+1) \rangle}{\langle P(0)P^\dagger(R) \rangle} \right]. \quad (3.17)$$

The lattice spacing in Fermi units is then

$$a = \frac{0.1973\text{GeV fm}}{\sqrt{0.440\text{GeV}}} \left[ -\frac{1}{L_T} \log \left( \frac{\langle P(0)P^\dagger(R+1) \rangle}{\langle P(0)P^\dagger(R) \rangle} \right) \right]^{\frac{1}{2}}, \quad (3.18)$$

on each gauge configuration.

To enhance the statistics in a gauge-independent way, the aforementioned expectation values are computed as the average across all lattice points. These observations serve as a test to see if we can accurately determine the lattice spacing  $a \simeq 0.098$  from two Polyakov loop correlators that are located at various distances. Using  $L_T = 36$  on the same lattice we obtain [156] an accurate lattice spacing value, which shows the insignificant impact of cross-correlations between close-proximity Polyakov loop correlators.

### 3.4 Cooling method

Our measurements of the action density distribution across the lattice are preceded by an ultraviolet (UV) filtering procedure. In order to achieve a decent signal-to-noise ratio in the aforementioned correlations, the UV-filtering of the gauge configurations suppresses the short-range quantum fluctuations of the vacuum. By diffusing the gauge links across the entire 4-dimensional lattice, a local action reduction occurs.

At large source separations, it was demonstrated that the effective string physics in the heavy meson is independent of the UV fluctuations [123]. With careful choice of the number of cooling sweeps it can be shown that the lattice data compares with the predictions of the free string model at the intermediate and large source separation distance at high temperatures [50].

As an alternative to [157, 158], who employed the Cabbibo-Marinari cooling method [154], we have chosen to cool the gauge field using a stout-link cooling algorithm [159]. Filtering techniques of this type are categorized within the set of the so-called analytic link-blocking methods.

The smearing algorithm can be describe as follows: Beginning with the sum of the two staples touching  $U_\mu(x)$  which reside in the  $\mu - \nu$  plane

$$\begin{aligned} \Sigma_{\mu\nu} &= U_\nu(x + \hat{\mu})U_\mu^\dagger(x + \hat{\nu})U_\nu^\dagger(x) \\ &+ U_\nu^\dagger(x + \hat{\mu} - \hat{\nu})U_\mu^\dagger(x - \hat{\nu})U_\nu(x - \hat{\nu}) \end{aligned} \quad (3.19)$$

define the weighted sum of the perpendicular staples which begin at lattice site  $x$  and terminate at neighboring site  $x + \hat{\mu}$

$$C_\mu(x) = \sum_{\substack{\nu \\ \nu \neq \mu}} \rho_{\mu\nu} \Sigma_{\mu\nu}^\dagger(x) \quad (3.20)$$

which defines the standard stout-link smearing [159]. The weights  $\rho_{\mu\nu}$  are tunable real parameters. Then the matrix  $Q_\mu(x)$ , defined in  $SU(3)$  by

$$Q_\mu(x) = \frac{i}{2} \left( \Omega_\mu^\dagger(x) - \Omega_\mu(x) \right) - \frac{i}{6} \text{Tr} \left( \Omega_\mu^\dagger(x) - \Omega_\mu(x) \right) \quad (3.21)$$



$n_{\text{sw}}$  is almost twice as large as the corresponding sweeps in APE smearing with a smearing parameter  $\alpha = 0.7$ .

**Table 1:** The characteristic smearing radius  $R_s$  Eq.(3.25) at each smearing level  $n_{\text{sw}}$ .

Number of smearing sweeps $n_{\text{sw}}$	20	40	60	80
Characteristic smearing radius $R_s$	0.27	0.38	0.47	0.54

The diffuseness model of the smearing procedure given by Eq. (3.25) establishes a characteristic radius that can be used to scale the effects of each smearing level. So one can find a mapping between the smearing radius and distance scales, for example, at which smearing effects can be neglected.

This distance scale could be established by a careful examination of a lattice observable such as the confining force among  $3Q$  system. In the next section we provide a detailed numerical evaluation of the potential of both  $(QQ)Q$  system at two temperature scales.

Many lattice measurements are affected by renormalization effects [162] via lattice spacing, which creates a natural cutoff for the underlying QFT. Cutoff and renormalization effects are entangled such that an energy scale inverse to the lattice spacing is set; hence, any change in the scale also affects the cutoff. A shift in the cutoff causes the width to be measured with a constant overall offset [45]. This deduction is based on the observation of

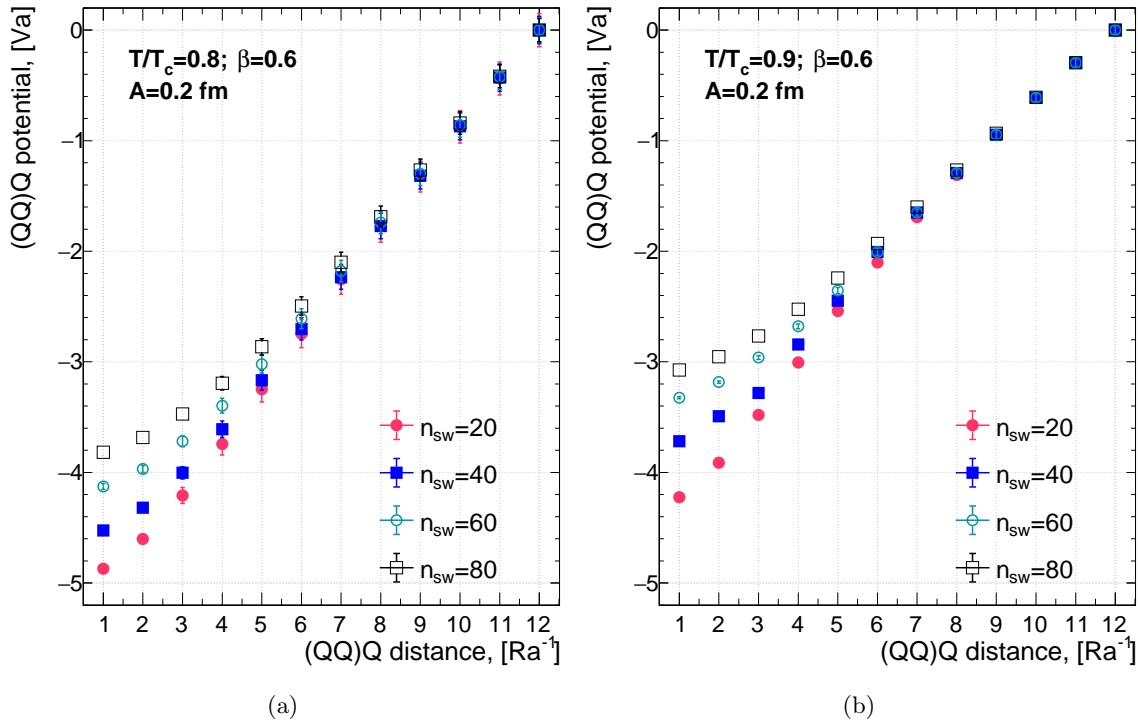


**Figure 5:** The  $3Q$  potential for a planar  $3Q$  arrangement such as that in Fig. 4 with bases  $A = 0.2$  fm versus the height  $R$  measured at the depicted cooling levels (a) Temperature  $T/T_c = 0.8$ , (b) Temperature  $T/T_c = 0.9$ .

an identical impact on the width when a different number of cooling sweeps are applied, which in turn increases lattice spacing or modifies the UV scale. In the configuration under scrutiny, we investigate the behavior of the IR quantum broadening of the width, which would not be impacted [50] by the identical global shifts.

The force [88] is a derived observable that can be calculated on the lattice from the potential through

$$F\left(R - \frac{a}{2}\right) = \frac{V(R) - V(R - a)}{a}, \quad (3.26)$$

with color source separation  $R$  and lattice spacing  $a$ , hence remove the overall renormalization change due to cooling. Otherwise one can normalize the potential with respect to a fixed point such as  $R = 1.2$  fm as shown in Fig.5.

Inspection of the potential of the diquark at the two considered temperatures, in Fig.5, reveals numerical outcomes measured after 40 cooling sweeps can be identified for heights  $R \geq 0.4$  fm are almost identical within the uncertainty of measurements. Similarly,  $n_{\text{sw}} \leq 60$  cooling sweeps at  $T/T_c = 0.8$  provide approximately forces on distance  $R \geq 0.5$ .

The above observational outcomes can be related to the cooling radius as discussed above. Table. 3.4 collects the characteristic radius of the Brownian motion at each selected number of sweeps. At both temperatures, the potential measured at triangle heights  $R \geq R_s$  receives a minimal impact of cooling at the number of sweeps  $n_{\text{sw}}$ .

#### 4. Diquark-quark (QQ)Q potential

To determine the heavy quarks potential for a planar  $3Q$  arrangement that corresponds to isosceles triangles with bases  $A$  and height  $R$ , as shown in the schematic Fig. 6, we analyse the correlators (3.3) corresponding to the meson and Eq.(3.6) to that of the baryon.

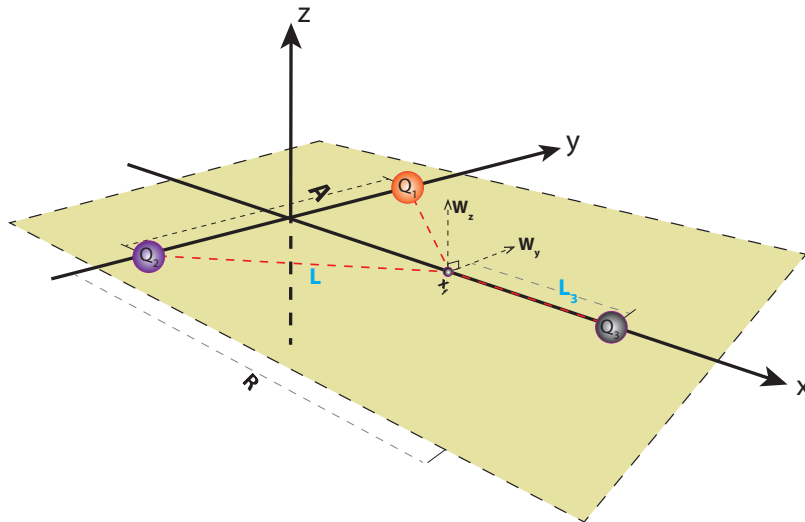


**Figure 6:** Schematic diagram showing the configuration of the  $Y$  string relative to the quark source positions. The junction's locus is fixed at Fermat point  $x_f$ . The isosceles base is denoted as  $A = 2d$ , the Fermat point is located at  $x_F = A/2\sqrt{3}$ .

Through the prescribed cooling method of the last section, the gauge configurations have been UV filtered. The number of sweeps gradually increased  $n_{\text{sw}} = 20, 40, 60$ , up to 80 sweeps. The two quarks  $Q_1$  and  $Q_2$  that make up the diquark system at the basis are interspersed with overlapping patches as a result of the link-fuzzing procedure (see Fig. 4) which has negligible impact on the potential measurement.

Nevertheless, for the sake of identifying the two systems one may still consider distances within the sphere of cooling among the  $Q_3$  and the diquark  $Q_1Q_2$ . It is interesting to find that while comparing the  $Q\bar{Q}$  and  $(QQ)Q$  systems with gauge connections subjected to the same number of cooling sweeps, we found the potential of the two systems conformally change with respect to each other with the application of the same number of UV filtering sweeps. That is, the data preserve the differences at a given isosceles height.

The numerical data for the meson and diquark-baryon are plotted in Fig.7(a) at the two close temperatures  $T/T_c \simeq 0.8$  (a) and  $T/T_c \simeq 0.9$ (b). The comparison in Fig.7(a) depicts the diquark-quark potential as the quark has pulled a distance  $R$  apart, the diquark diameter is  $A = 0.2$  fm and the number of stout-link cooling correspond to  $n_{\text{sw}} = 80$ .

At a temperature near the end of the QCD Plateau,  $T/T_c = 0.8$ , we find that the diquark-quark configuration exposes an identical potential to the mesonic string. At this temperature, thermal factors only account for around 10% of the decrease in string tension [126]. This outcome is highly pertinent to the analysis performed in Ref. [142] which displays diquark-baryon identical to meson configuration, at a much lower temperature using a lattice of  $N_t = 20$  time slices and  $\beta = 6.0$ .

The numerical values for the Polyakov loop correlators corresponding to each system, however, differ noticeably close to the deconfinement point  $T/T_c = 0.9$ . The remarkable findings are that the  $(QQ)Q$  quark does not display the symmetry in the confining potential with the meson at either short or intermediate distance scales from the triangle base  $R < 1.0$  fm, as shown in Fig.7(b).

Thus, a splitting of the symmetrical confining force inside the bosonic and fermionic arrangements does occur with the rise of the temperature scale. At this point, we are naturally inclined to question both the meson-like and baryon-like aspects of each system. The effective bosonic string models are a well-suited framework to further explore the behavior of the lattice data. Within this paradigm, for example, one can pose the question: If the mesonic gluonic field of the diquark is excited, would a crossover into the Y-junction behavior take place?

In the baryon, the analysis of the lattice data would suggest two types of parametrization depending on the interquark distances, i.e., the  $\Delta$  and Y-type potentials. [131, 146, 163, 164]. The  $\Delta$ -potential describes a sum of two-body forces and is proportional to the perimeter of the  $3Q$  triangle with a string tension half that of the corresponding  $Q\bar{Q}$  system. The  $\Delta$ -potential is given by

$$V_{3Q}(\vec{r}_1, \vec{r}_2, \vec{r}_3) = -\frac{1}{2}A_{Q\bar{Q}} \sum_{i<j} \frac{1}{|\vec{r}_i - \vec{r}_j|} + \frac{1}{2}\sigma_{Q\bar{Q}} \sum_{i<j} |\vec{r}_i - \vec{r}_j|, \quad (4.1)$$

with  $A_{Q\bar{Q}}$  signifying the strength of the one-gluon-exchange (OGE) Coulomb term derived from perturbative QCD (see Ref. [131, 146]).

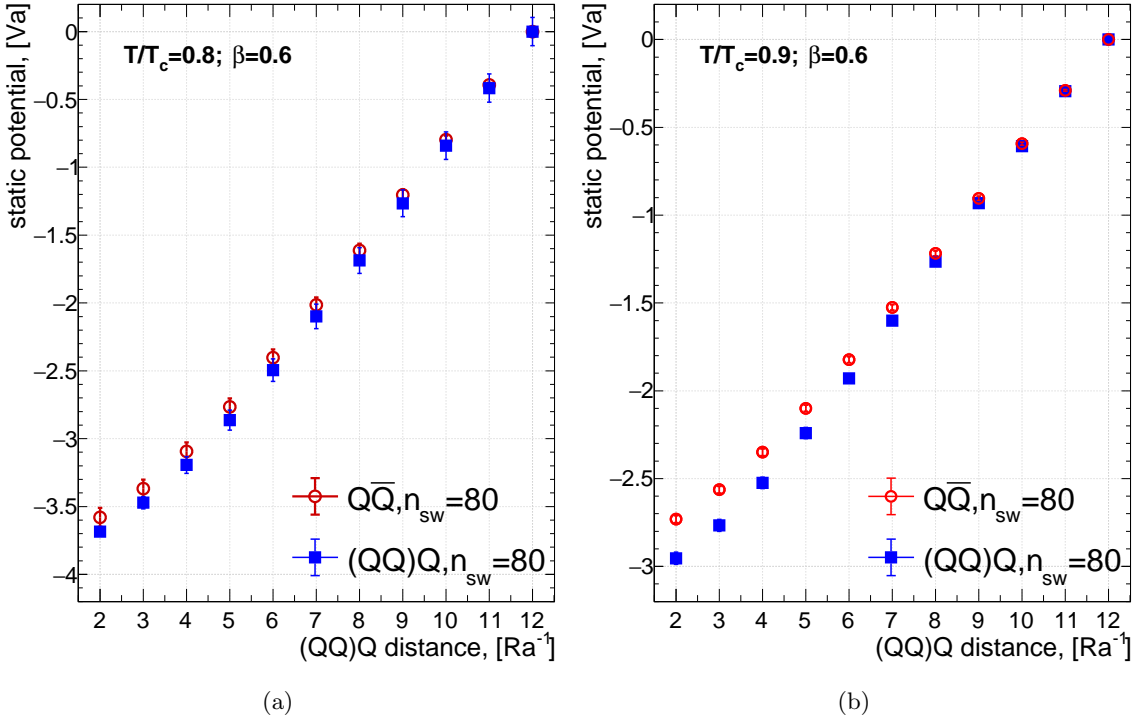


**Figure 7:** (a) Compares of the static potential of quark-antiquark  $Q\bar{Q}$  and diquark-quark  $(QQ)Q$  configuration of base length  $A = 0.2$  fm at  $T/T_c = 0.8$  and  $\beta = 6.0$ . (b): Compares of the static potential of quark-antiquark  $Q\bar{Q}$  and diquark-quark  $(QQ)Q$  configuration of base length  $A = 0.2$  fm at  $T/T_c = 0.9$  and  $\beta = 6.0$ .

Conversely, the Y-potential models a three-body force that is proportional to the shortest length of the three strings and has the same string tension as the  $Q\bar{Q}$  system. In this picture, the three-body force is conceived as a result of the formation of a Y-shaped string linking the three-static quarks. Sub-leading modifications to the potential are produced as a result of the quantum fluctuations of the Y-string, and these corrections are anticipated to be enhanced at high temperatures. Formula Eq.(2.33) sums up the contributions to the  $3Q$  potential resulting from both the perpendicular and in-plane fluctuations as discussed in section (II).

At the considered two temperatures scales, the three-quark system exhibits a  $\Delta$ -shaped energy-density distribution [39]. This does not rule out that the  $\Delta$ -shaped action density can manifests as a result of the fluctuations of the junction of an underlying Y-string [39]. To thoroughly gain insight into the configuration of the strings binding the constituent quarks, we draw a comparison between the  $\Delta$ -ansatz parameterization Eq.(4.1) and the Y-string model Eq.(2.33).

We systematically examine each model on a selected  $3Q$  configuration with a significant separation between the two quarks  $Q_1$  and  $Q_2$ . We consider data corresponding to the potential of an isosceles  $3Q$  quark configuration with base length  $A = 0.8$  fm at the highest temperature  $T/T_c = 0.9$ . The fits are obtained by optimizing the UV-parameter space  $\mu$

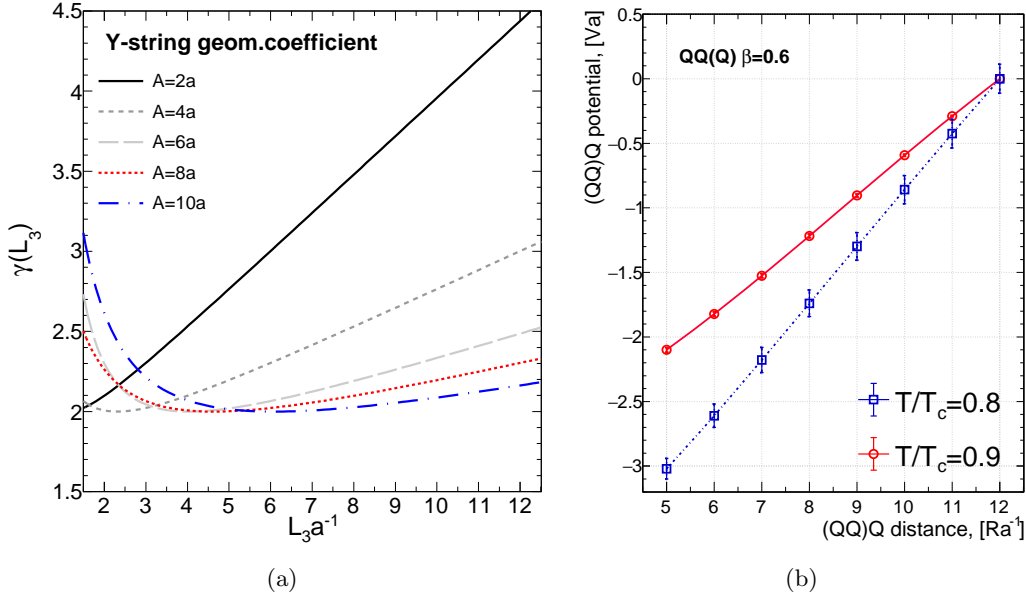


**Figure 8:** (a) The geometrical coefficient  $\gamma$  which determine the strength of the quantum fluctuations of the baryonic Y-string Eq.(2.33)(b)The  $3Q$  potential versus the height length of isosceles triangular configuration of the planar  $3Q$  with bases of length  $A = 0.8$  fm. The lines correspond to the  $3Q$  potential according to the best fits to the string picture formula of Eq.(2.33) at  $T/T_c = 0.8$  and  $T/T_c = 0.9$  over for fit interval range  $R \in [5a, 12a]$ .

in the above-mentioned models such that the least-square residuals

$$\chi^2(\mu) = \sum_i \left( \frac{(V(R_i) - V_{model}(R_i; \mu))}{e_i(R_i)} \right)^2, \quad (4.2)$$

is minimized, where  $e(R_i)$  is the standard error in the measured potential  $V(R_i)$  from the lattice simulation.

**Table 2:** The returned  $\chi_{\text{dof}}^2(x)$  for fits of the lattice data to  $3Q$  isosceles of width  $A = 0.6$  fm at  $T/T_c = 0.9$ . The fits compare Eq.(4.1) for the  $\Delta$ -ansatz, Eq.(2.33) for the Y-string model and Eq.(4.4) for a Coulomb Y-ansatz. Measurements are taken on  $n_{\text{sw}} = 20$  sweeps of cooling.

Fit Range	$R \in [3 - 12]$		$R \in [4 - 12]$		$R \in [5 - 12]$	
Fit Parameters	$\chi^2$	$\sigma_0 a^2$	$\chi^2$	$\sigma_0 a^2$	$\chi^2$	$\sigma_0 a^2$
$\Delta$ -ansatz	33.4	0.362(4)	22.4	0.352(3)	13.0	0.341(5)
Y-string model	16.9	0.347(3)	11.8	0.339(5)	6.5	0.329(6)
Y-Coulomb	10.1	0.325(3)	10.0	0.324(3)	7.5	0.318(6)

Before fitting this string potential to the lattice data, the Y-string's length should be minimized, i.e., with the node's position at the Fermat point of the  $3Q$  triangular configuration. With simple variational calculus, the position of the Fermat point of the planar isosceles arrangement can easily be shown, see Fig. 6, to lie at  $x_f = \frac{A}{2\sqrt{3}}$ . The

geometrical coefficient in Eq.(2.33) is evaluated as

$$\gamma(L_1, L_3) = 2 + \frac{24L_Y}{\pi} \left[ -\frac{\pi}{12L_1} - \frac{\pi}{24L_3} + \frac{1}{2\pi} \int_0^\infty d\omega \ln \left( \frac{2}{3} \coth(\omega L_1) + \frac{1}{3} \coth(\omega L_3) \right) \right]. \quad (4.3)$$

Fig.8(a) shows the variation of the above geometrical coefficient with the length of the three strings  $L_i$ .

In Table 4 we collected the returned values of  $\chi^2$  from the resultant fits of the  $3Q$  potential to the Y-string model formula Eq.(2.33) and  $\Delta$ -model Eq.(4.1). The string tension has been taken as a fit parameter together with ultraviolet (UV)-cutoff  $\mu$ .

With the fit range including all the considered points  $R \in [5, 12]$ , the Y-string model returns the best fit compared to the  $\Delta$ -model. It is interesting to find that even the Coulumbic Y-model [131, 146], given by

$$V_{3Q}(\vec{r}_1, \vec{r}_2, \vec{r}_3) = -\frac{1}{2} A_{Q\bar{Q}} \sum_{i < j} \frac{1}{|\vec{r}_i - \vec{r}_j|} + \sigma_{Q\bar{Q}} L_Y, \quad (4.4)$$

returns slightly higher values of  $\chi^2$  compared to the Y-string model, see Table 4. For locations containing just long isosceles heights,  $R \in [8, 12]$ , and shorter isosceles heights,  $R \in [5, 8]$ , the Y-string model still provides the best fit over this middle-length scale. A consistent physical realization of this observation is that the three-body force receives subleading modifications which are consistent with these owing to the junction fluctuations.

Fig. 8(b) depicts the  $3Q$  potential versus the height length of the isosceles triangle configuration with  $A = 0.8$  fm. According to the best fits to the string picture formula of Eq.(2.33) at the two temperatures.

At large  $Q_3$  source separation, small variations are noticed in the value of  $\chi^2$  returned from the fits corresponding to the two confining potential ansatz, i.e., the Y-string and the other models. This also the case for base width  $A = 0.2$  fm of the diquark-quark which is small enough to replicate the same fit behavior. In other words, the minimal length of the Y-string gives a node location close to the third side of an isosceles triangle, which roughly has analogous effect to a  $\Delta$ -string on the circumference.

Nevertheless, the Y-string model appears as the most suitable framework for discussing the fine structure of the bayonic characteristics of a particular  $3Q$  configuration. In what follows we oppose the Y-string model and its mesonic counterpart while discussing the diquark-baryon data.

Since we are interested in spotting mesonic string signatures of  $(QQ)Q$  system, a fit of the mesonic string potential Eq.(2.14) to the diquark-quark potential data is considered. The fits return the  $\chi^2$ , string tension and  $\sigma_0 a^2$  values shown in Table. 3. The fits are performed at both temperatures with the string tension taken as a fit parameter.

It should be noted that the quark-antiquark string at  $T/T_c = 0.9$  retrieves [53] a string tension parameter  $\sigma a^2 = 0.0365$  that is different from that  $\sigma_0 a^2 = 0.044$  at the lower temperature  $T/T_c = 0.8$  and  $T = 0$  [142]. However, these values would be reproduced in the meson from the mesonic string potential only if other effects beyond the free string model [53] are included, such as self-interaction [101, 103], rigidity [165, 166] and boundary effects [103].

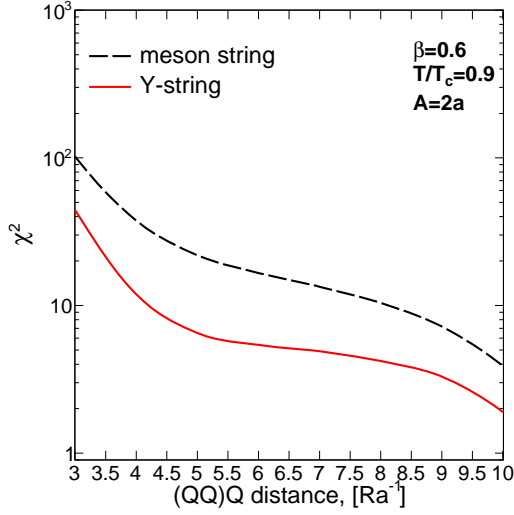


**Figure 9:** The returned  $\chi^2$  from the fits of mesonic and baryonic strings Eq.(2.33) to the the data of the  $(QQ)Q$  diquark-quark potential. The fits are performed on intervals  $R \in [R_m, 1.2]$  fm. The temperature scale  $T/T_c = 0.9$  and the diquark diameter is  $A = 0.2$  fm.

**Table 3:** Lists the returned values of the  $\chi_{\text{dof}}^2$  for fits of the lattice data to the mesonic string model formula Eq.(2.14), the fits are for isosceles three-quark configurations of base width  $A = 2a$  and  $A = 4a$  at  $T/T_c = 0.8$ . Measurements are taken after  $n_{\text{sw}} = 40$  sweeps of cooling.

Fit range $R \in [R_m, R_M]$ Fit parameters	[3 – 12]		[4 – 12]		[5 – 12]	
	$\chi^2$	$\sigma_0 a^2$	$\chi^2$	$\sigma_0 a^2$	$\chi^2$	$\sigma_0 a^2$
$A = 2a$	5.40	0.041(1)	3.04	0.045(1)	0.39	0.045(1)
$A = 4a$	13.87	0.39(5)	4.21	0.040(5)	7.68	0.044(5)

The fit of the mesonic string potential Eq.(2.16) to the diquark-quark data, with a fixed value of  $\sigma_0 a^2 = 0.0365$  at  $T/T_c = 0.9$  [41], is shown in Fig.9. The returned  $\chi^2$ 's, collected in Table 4, are plotted versus the minimal isosceles height  $R_m$  such that the fit interval is  $R \in [R_m, 1.2]$  fm. The lines compare the fit of the Y-string formula of Eq.(2.33) and mesonic string for each fit interval at the same string tension of  $\sigma_0 a^2 = 0.0365$  of the  $QQ\bar{Q}$ .

Fig. 23 displays the fast change in the residuals to good values when the diquark data are fitted into the Y-string model. The mesonic string, however, returns poor values of  $\chi^2$  even by the exclusion of data points corresponding to short isosceles height. The lattice data best agrees with the baryonic Y-string formulated of Eq.(2.33) suggests that the junction impacts take place at temperatures closer to the deconfinement point  $T/T_c = 0.9$ .

The fit of the mesonic string potential Eq.(2.16), with a fixed value of  $\sigma_0 a^2 = 0.036$  at  $T/T_c = 0.9$ , is shown in Fig.10(a). A drastic deviation of the model from the lattice data of the diquark-quark system is evident. It's interesting that the string tension from the fits of the baryonic string model, on the other hand, matches the value returned at  $T = 0$  [142].

At the lower temperature scale  $T/T_c = 0.8$ , both fits to the diquark-quark potential

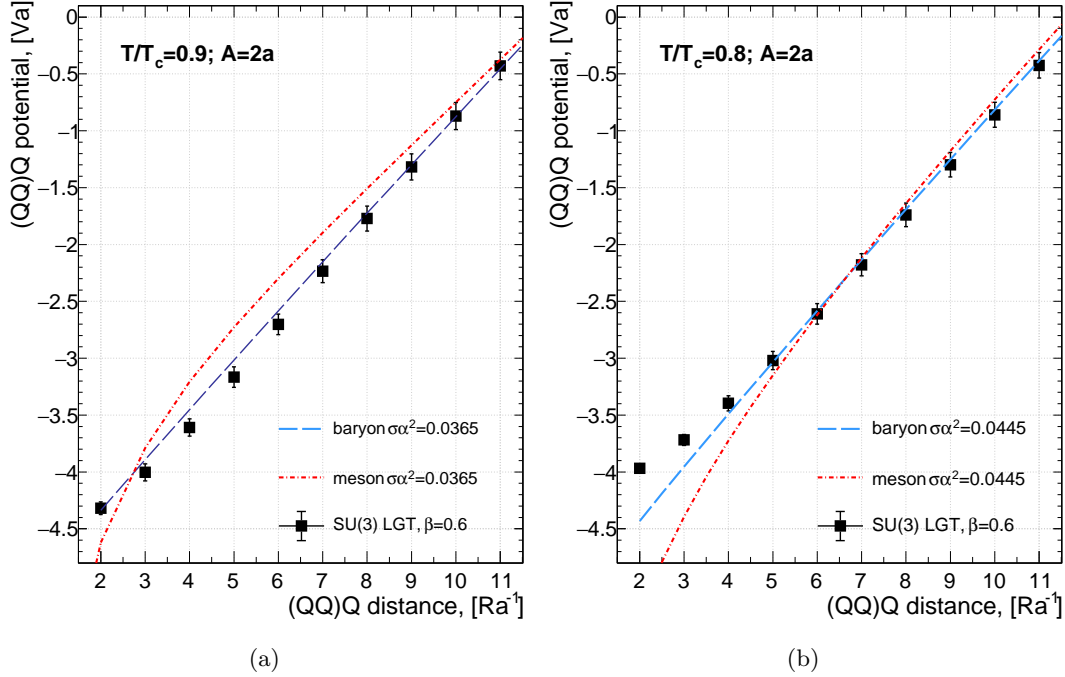


**Figure 10:** The  $(QQ)Q$  diquark-quark potential versus the height length of configuration of the planar quark system with diquark diameter  $A = 0.2$  fm. The lines compares the fit of Eq.(2.33) for the baryonic potential and that of the mesonic string Eq.(2.14). The fit interval over range  $R \in [10a, 12a]$  in (a).

data for the mesonic string Eq.(2.14) and that of the baryonic junction model are contrasted in Fig. 10(b). The plot shows that both string models provide the same string tension value,  $\sigma_0 a^2 = 0.045$ , and that they both agree well with the potential data of diquark-quark system. The value of the string tension is the same as the  $Q\bar{Q}$  system's value at the same temperature.

**Table 4:** The returned  $\chi_{\text{dof}}^2(x)$  for fits of the lattice data to  $3Q$  isosceles of width  $A = 0.2$  fm at  $T/T_c = 0.9$ . The fits compare fits to Eq.(2.33) for the Y-string model and with the fits to the mesonic string Eq.(2.14). Measurements are taken on  $n_{\text{sw}} = 20$  sweeps of cooling.

Fit Range	$R \in [3 - 12]$	$R \in [4 - 12]$	$R \in [5 - 12]$	$R \in [6 - 12]$
Y-string model	44.5	11.9	6.5	5.4
Mesonic String	102.1	37.6	21.9	16.6

Despite of the large values of  $\chi^2$  when the fit interval includes points of short heights  $R = [0.3, 1.2]$  fm. Nevertheless, the fit to the baryonic Y-string model, with a fixed value of the  $\sigma_0 a^2 = 0.0365$ , shown in Fig.10(a) still reflects an improved overall parameterization behavior over the mesonic counterpart even for fits on small fit intervals such as  $R \in [10a, 12a]$ .

So far we examined the mesonic string models on the baryonic data of diquark-quark

$(QQ)Q$ . We then looked at the Y-baryonic strings models that fit the mesonic data  $(Q\bar{Q})$ . In conclusion, the potential of the gluonic string binding the  $(QQ)Q$  configuration, approximated with a diquark diameter  $A = 0.2$  fm, on the QCD Plateau up to the temperature  $T/T_c = 0.8$  exhibits the same behavior as that of the quark-antiquark  $Q\bar{Q}$ .

The further rise of the temperature causes the bosonic and fermionic arrangements to lose their symmetry. Close to the critical point  $T/T_c = 0.9$  the data analysis of the potential shows a change in the slope of the diquark data. We find through the fits that a Y-string model rather than a mesonic string is more likely to represent the diquark-quark data down this scale.

## 5. Diquark-quark $(QQ)Q$ energy profile

### 5.1 Vacuum's Action-density

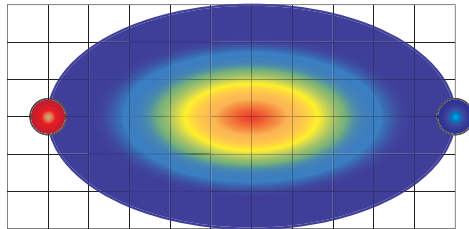


**Figure 11:** The action density Eq.(3.12) of meson  $Q\bar{Q}$  at  $T/T_c = 0.8$  and color source separation  $R = 1.2$  fm measured after  $n_{sw} = 60$ .

Further characteristics of the confining force can be explored by analyzing the profiles of the flux tubes. We examine the action density of the vacuum in the presence of quarks through the correlation coefficients  $\mathcal{C}_{3Q}(\vec{\rho})$  and  $\mathcal{C}_{Q\bar{Q}}(\vec{y})$  of Eq. (3.12) and Eq. (3.15). The correlations correspond to  $Q\bar{Q}$  and the  $(QQ)Q$  systems where the vector  $\vec{\rho} = (x, y, 0)$  is constrained to the plane of the color sources and its perpendicular plane  $\vec{\rho} = (x, 0, z)$ . The location of the quark is at position  $(x, 0, 0)$  with  $R = x$  is made to vary from  $R = a$  to  $R = 12a$  steps for each selected separation  $A$  of the base quarks. Due to probable correlations from the other side of the lattice caused by the periodic boundary, the color source separation  $R \geq 1.2$  fm should be discarded in a careful analysis.

Figs.11 and 12 display two snap-shots of the expulsion of vacuum fluctuations at  $T/T_c = 0.8$  and  $R = 1.0$  fm. The density profile corresponds to the formation of flux-tubes of both quark-antiquark and diquark-quark configurations.

The action density distribution within the quark-antiquark system is not uniformly distributed. The planar distribution  $\mathcal{C}_{Q\bar{Q}}(\vec{\rho}(x, y, z = 0)) = 0$  shows a peak maximum at the center of the distribution. The center line  $\vec{\rho}(x, y = 0, z = 0)$  corresponding to the x-axis acquires an action-density maximal curve. The diquark-quark system in Fig. 12(a); however, discloses a maximum curve  $\mathcal{C}_{3Q}(\vec{\rho}(x, y = 0, z = 0))$  that peaks at a point displaced one lattice spacing from the center towards the diquark [52, 123].

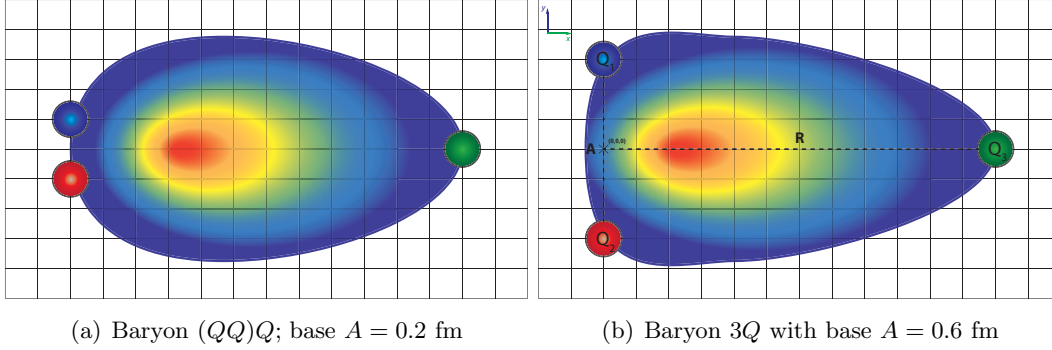


**Figure 12:** The baryonic action density Eq.(3.15) with the decrease of the two quark  $(QQ)$  separation at the planar-triangle base from  $A = 6a$  to  $A = 6a$  and the formation of quark-antiquark gluonic field at  $T/T_c = 0.8$

Patterns of the action density at higher temperature  $T/T_c = 0.9$  are represented in Figs. 13 and 14. The planar map shows the action density in the quark plane for sources  $Q_3$  with separations of  $R = 1.4$  fm. The flux density is displayed in the projection plane- $yx$  for separation distance between the quarks  $Q_1$  and  $Q_2$  corresponding to a base length  $A = 0.2$  fm shown in Fig. 14(a) and  $A = 0.6$  fm in Fig. 14(b).

We display the action density in a 2D-plane for source separations of  $R = 0.6, 0.9, 1.2,$

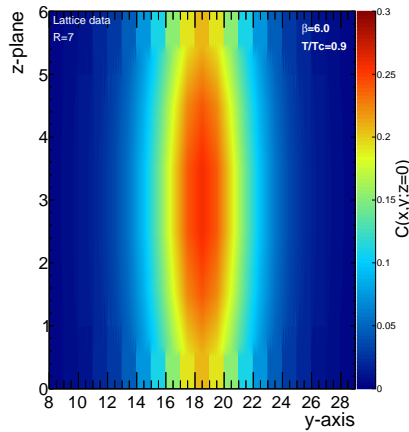


**Figure 13:** The in-plane action density Eq.(3.12) for meson  $Q\bar{Q}$  at  $T/T_c = 0.9$  and color source separation  $R = 1.4$  fm,  $n_{sw} = 40$ .

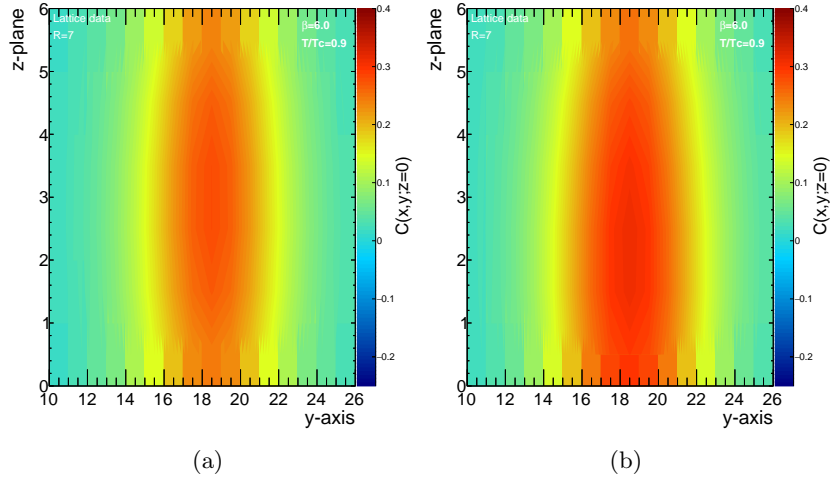


**Figure 14:** The in-plane action density Eq.(3.12) for baryon  $(QQ)Q$  at  $T/T_c = 0.9$ . The baryonic geometry correspond to a triangle with isosceles height  $R = 1.4$  fm and base length  $A = 0.2$  fm in (a) and  $A = 0.4$  fm in (b).

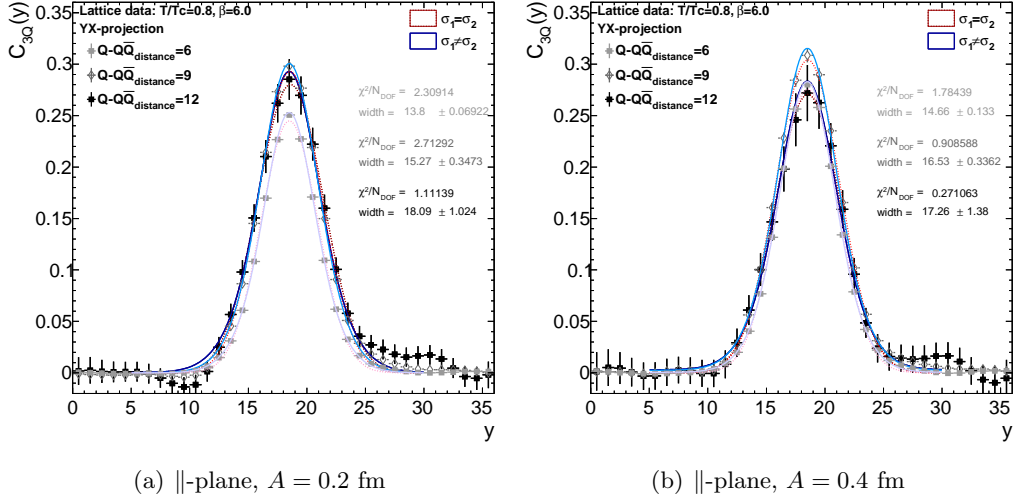


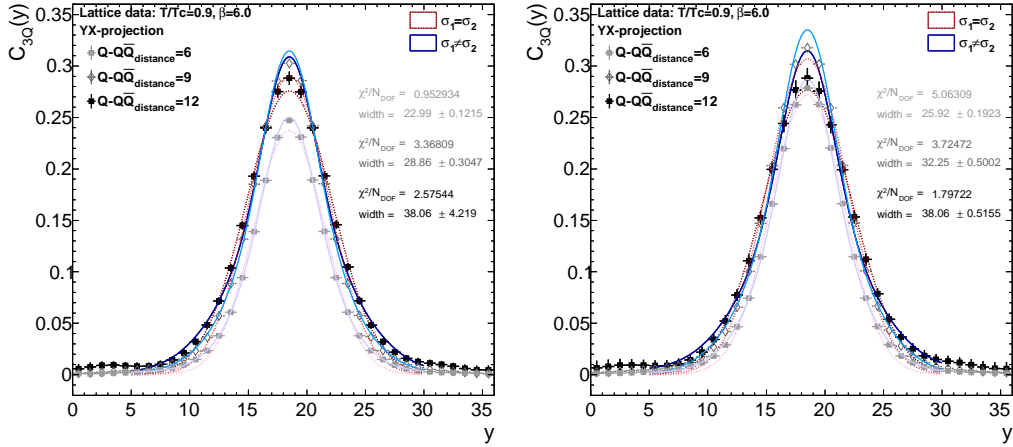
**Figure 15:** The action density distribution  $C_{3Q}(r, \theta, x = R/2)$  at the center of the tube Eq.(3.15),  $R/2$ , for source separations  $R = 0.6, 0.9, 1.2$  fm and temperature  $T/T_c \approx 0.8$ . The red dotted lines correspond to fits with the standard Gaussian distribution, assuming  $\sigma_1 = \sigma_2$  in Eq.(5.1), the blue solid lines correspond to unconstrained form,  $\sigma_1 \neq \sigma_2$ . The distance between  $Q_1$  and  $Q_2$  quarks denoted as  $A = 2d$ , see Fig.4 for details. Transverse profiles for the quark-diquark system are denoted as  $yx$ -plane, and the longitudinal flux tube profiles are denoted as  $||$ -plane.

and 1.4 fm in Appendix. A. In Fig. 25 and 26 correspond to the action density at temperature  $T/T_c = 0.9$  and  $T/T_c = 0.8$ . The panels compare the action density in the quark plane and also in the perpendicular plane, with the bases length and  $A = 0.2$  fm corresponding to diquark-quark system at  $A = 0.4$  fm from the  $Q$ .

We consider the longitudinal profiles of quark-diquark and quark-antiquark flux tubes along the axis  $\vec{r} = (x, 0, 0)$  in Fig. 13. The vacuum expulsion is stronger near the diquark

**Table 5:** The mean-square width  $W^2$  and amplitude of the in-plane and perpendicular action-density measured at the corresponding planes using fits to a double-Gaussian ansatz Eq.(5.1) at temperature  $T/T_c = 0.9$  and  $n_{\text{sw}} = 40$ .

plane $n = R/a$	$x = 1$			$x = 2$			$x = 3$			$x = 4$			
	$A$	$w^2 a^{-2}$	$\chi^2_{\text{dof}}$	$A$	$w^2 a^{-2}$	$\chi^2_{\text{dof}}$	$A$	$w^2 a^{-2}$	$\chi^2_{\text{dof}}$	$A$	$w^2 a^{-2}$	$\chi^2_{\text{dof}}$	
$R = 4a$	$QQ$	0.0654(1)	17.75(5)	4.3	0.0711(1)	17.27(5)	4.40	0.0654(1)	17.75(5)	4.3			
	$(QQ)Q_{\parallel}$	0.0837(2)	24.92(7)	5.8	0.0864(2)	24.59(7)	5.74	0.0810(2)	25.03(7)	5.84			
	$(QQ)Q_{\perp}$	0.0833(2)	24.93(6)	8.13	0.0862(2)	24.63(6)	8.57	0.0810(2)	25.03(7)	10.51			
$R = 5a$	$QQ$	0.0777(2)	18.75(6)	3.98	0.0894(2)	17.97(6)	4.03	0.0894(2)	17.97(5)	4.3	0.0777(2)	18.75(6)	3.98
	$(QQ)Q_{\parallel}$	0.1(2)	27.22(7)	239.03	0.1064(2)	24.20(7)	4.87	0.1053(2)	24.24(7)	5.10	0.0951(2)	24.71(7)	5.33
	$(QQ)Q_{\perp}$	0.0986(2)	24.81(7)	7.09	0.1062(2)	24.27(7)	6.83	0.1052(2)	24.23(7)	7.68	0.0952(2)	24.83(7)	9.45
$R = 6a$	$QQ$	0.0842(2)	20.28	3.27	0.1003(2)	19.31(7)	3.2	0.1062(3)	19.04(6)	3.1	0.0843(2)	19.3(6)	3.21
	$(QQ)Q_{\parallel}$	0.1097(3)	24.93(9)	2.98	0.1212(3)	24.67(9)	3.51	0.1245(3)	24.57(9)	3.86	0.1190(3)	24.67(8)	4.30
	$(QQ)Q_{\perp}$	0.1092(3)	25.47(8)	5.10	0.1209(3)	24.82(8)	5.19	0.1243(3)	24.58(8)	5.17	0.1190(3)	24.73(8)	5.98
$R = 7a$	$QQ$	0.0867(3)	22.1(2)	2.5	0.1048(3)	21.04(8)	2.47	0.1147(4)	20.64(9)	2.3	0.0867(3)	20.64(9)	2.3
	$(QQ)Q_{\parallel}$	0.1161(3)	25.7(1)	1.6	0.1306(4)	25.6(1)	2.15	0.1449(6)	26.7(1)	1.44	0.1367(5)	25.5(1)	3.02
	$(QQ)Q_{\perp}$	0.1156(3)	26.6(1)	5.20	0.1303(4)	25.9(1)	4.02	0.1448(6)	27.0(1)	2.35	0.1366(5)	25.5(1)	3.48
$R = 8a$	$QQ$	0.9(2)	24.1(1)	1.94	0.1049(4)	23.03(1)	1.91	0.1165(5)	22.6(1)	1.71	0.1206(5)	22.5(1)	1.62
	$(QQ)Q_{\parallel}$	0.1195(4)	26.5(1)	0.74	0.1354(5)	26.6(1)	1.10	0.1449(6)	26.7(1)	1.44	0.1476(6)	26.8(1)	1.83
	$(QQ)Q_{\perp}$	0.1190(4)	27.9(1)	4.67	0.1351(5)	27.3(1)	3.32	0.1448(6)	27.0(1)	2.35	0.1475(7)	26.9(1)	2.00
$R = 9a$	$QQ$	0.0856(4)	26.2(2)	1.38	0.1025(5)	25.2(2)	1.43	0.1140(6)	24.9(2)	1.30	0.1199(7)	24.9(2)	1.17
	$(QQ)Q_{\parallel}$	0.1209(5)	27.4(2)	0.33	0.1368(6)	27.6(2)	0.49	0.1474(8)	28.0(2)	0.48	0.1524(8)	28.3(2)	0.96
	$(QQ)Q_{\perp}$	0.1204(5)	29.2(2)	4.11	0.1366(7)	28.8(2)	2.92	0.1473(8)	28.6(2)	1.79	0.1523(9)	28.6(2)	1.21
$R = 10a$	$QQ$	0.0840(5)	28.26	0.91	0.0992(6)	27.6(2)	0.98	0.1094(8)	27.6(2)	0.91	0.1151(9)	27.8(2)	0.83
	$(QQ)Q_{\parallel}$	0.1210(6)	28.3(2)	0.17	0.1361(8)	28.6(2)	0.20	0.1464(9)	29.1(1)	0.20	0.152(1)	29.8(2)	0.46
	$(QQ)Q_{\perp}$	0.1205(7)	30.4(2)	3.27	0.1359(8)	30.1(2)	2.52	0.146(1)	30.2(2)	1.5	0.152(1)	30.4(2)	0.80
$R = 11a$	$QQ$	0.0821(7)	30.3	0.57	0.0953(8)	29.9(3)	0.6	0.1038(9)	30.3(3)	0.55	0.1084(1)	31.1(3)	0.50
	$(QQ)Q_{\parallel}$	0.1205(8)	29.5(3)	0.09	0.134(1)	29.6(3)	0.09	0.143(1)	30.2(3)	0.14	0.149(1)	31.2(3)	0.22
	$(QQ)Q_{\perp}$	0.1199(8)	31.5(3)	2.21	0.134(1)	31.3(1)	1.95	0.143(1)	31.6(3)	1.27	0.149(1)	32.2(3)	0.61
$R = 12a$	$QQ$	0.0799(8)	32.1(4)	0.34	0.0910(9)	32.0(4)	0.34	0.097(1)	33.0(4)	0.29	0.101(1)	34.6(4)	0.24
	$(QQ)Q_{\parallel}$	0.119(1)	31.2(4)	0.08	0.131(1)	30.9(4)	0.06	0.138(1)	31.3(4)	0.07	0.143(2)	32.4(4)	0.12
	$(QQ)Q_{\perp}$	0.119(1)	32.8(4)	1.21	0.131(1)	32.5(4)	1.28	0.138(1)	33.0(4)	0.97	0.143(2)	33.9(4)	0.49



(a)  $\parallel$ -plane,  $A = 0.2$  fm

(b)  $\parallel$ -plane,  $A = 0.4$  fm

**Figure 16:** Same as Fig.15. However, the temperature scale is set to  $T/T_c = 0.9$ .

than it is near the quark although we reported the same potential in the previous section. The two flux tubes, however, exhibit almost similar profiles close to the quark.

The transverse profiles are then inspected along a line that is orthogonal to the flux

**Table 6:** The mean-square width  $W^2$  and amplitude of the in-plane and perpendicular action-density measured at the middle plane  $R/2$  using fits to a double-Gaussian ansatz Eq.(5.1) at temperature  $T/T_c = 0.8$  and  $n_{\text{sw}} = 60$ .

	plane	$A$	$w^2 a^{-2}$	$\chi_{\text{dof}}^2$
$R = 4a$	$QQ$	0.0752(1)	14.21(5)	2.29
	$(QQ)Q_{\parallel}$	0.0937(2)	14.57(5)	1.60
	$(QQ)Q_{\perp}$	0.0936(2)	14.33(6)	1.30
$R = 5a$	$QQ$	0.1066(2)	14.51(5)	0.51
	$(QQ)Q_{\parallel}$	0.1171(2)	12.89(1)	15.91
	$(QQ)Q_{\perp}$	0.1183(3)	14.73(7)	1.22
$R = 6a$	$QQ$	0.1332(3)	15.11	0.23
	$(QQ)Q_{\parallel}$	0.1416(3)	15.35(7)	1.02
	$(QQ)Q_{\perp}$	0.1415(4)	15.17(8)	0.99
$R = 7a$	$QQ$	0.1530(5)	15.89(9)	0.07
	$(QQ)Q_{\parallel}$	0.1607(5)	15.9(1)	1.15
	$(QQ)Q_{\perp}$	0.1606(5)	16.0(1)	0.99
$R = 8a$	$QQ$	0.1721(9)	16.8(1)	0.02
	$(QQ)Q_{\parallel}$	0.1768(9)	16.4(2)	0.73
	$(QQ)Q_{\perp}$	0.1768(7)	16.6(1)	0.89
$R = 9a$	$QQ$	0.183(2)	18.0(2)	0.005
	$(QQ)Q_{\parallel}$	0.188(1)	17.0(2)	0.85
	$(QQ)Q_{\perp}$	0.1879(9)	17.8(2)	1.14
$R = 10a$	$QQ$	0.193(2)	19.6(3)	0.003
	$(QQ)Q_{\parallel}$	0.196(2)	17.6(4)	0.57
	$(QQ)Q_{\perp}$	0.196(1)	18.8(2)	1.14

tube's midpoint, *i.e.*, along  $(x/2, y, 0)$  for  $x$  even, or along  $((x+1)/2, y, 0)$  for  $x$  odd. We present profiles of diquark-quark and quark-antiquark flux tubes for  $x = 12$  in Fig. 12. We come upon that the transverse profiles are nearly identical as long as  $x$  is more than one-third of the length of the quark-antiquark system.

Apart from the qualitative aspects of the revealed density distribution of the QCD vacuum, a careful look into the rendered action density suggests extracting its numerical characteristics such as the moments of the distribution. A measurement of the width of the Euclidean action density may be then taken by fitting the density distribution  $\mathcal{C}(\vec{\rho}; x)$  to a suitable functional form.

Through each transverse plane to the cylinder's axis  $z$  we select a double-Gaussian function of amplitude  $A$  and fit parameters  $\sigma_1$ ,  $\sigma_2$  and  $\kappa$  such that

$$G(r, \theta; x) = A(e^{-r^2/\sigma_1^2} + e^{-r^2/\sigma_2^2}) + \kappa, \quad (5.1)$$

with  $r^2 = x^2 + y^2$  in each selected transverse plane  $\vec{\rho}(r, \theta; z)$ , which returns acceptable values of  $\chi^2$  at the intermediate and long distances [41]. The axial cylindrical symmetry of the tube is taken into account when estimating the mean-square width of the gluonic action

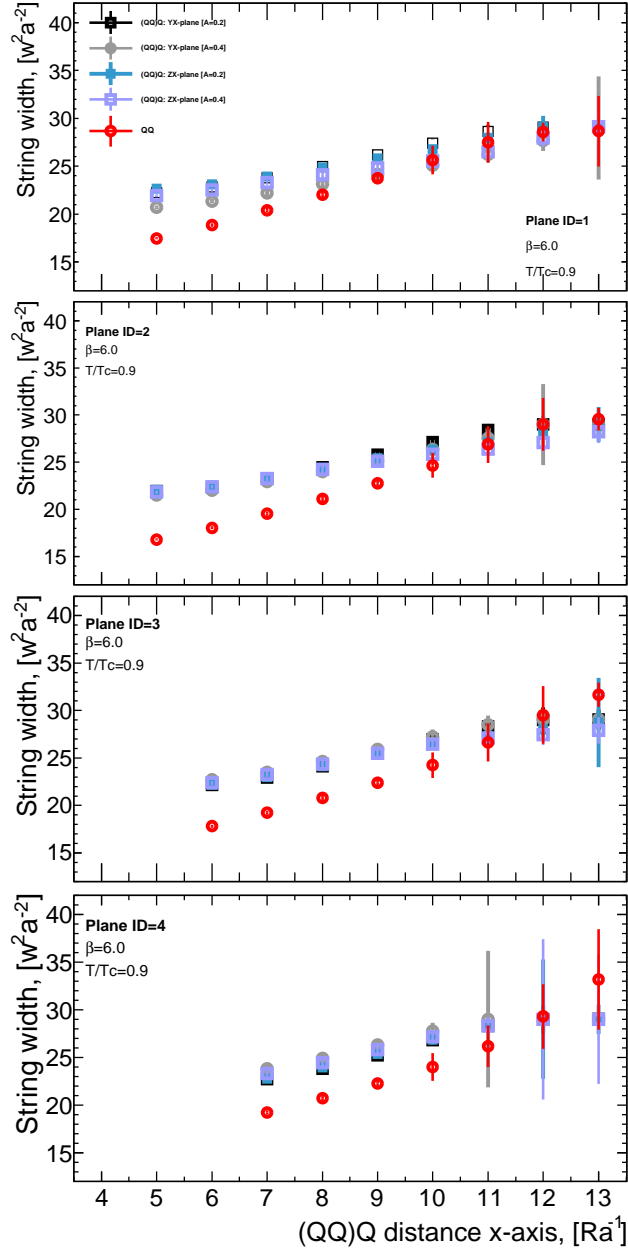


**Figure 17:** The in-plane and perpendicular-plane mean-square width at  $T/T_c = 0.9$  for  $(QQ)Q$  and  $QQ$  systems at planes  $x = 1, 2, 3$  and  $x = 4$ ,  $n_{sw} = 40$ .

density along each transverse plane to the quark-antiquark axis. In the  $Q(QQ)$  system this is not necessarily the case [38, 39] and a width measurement should be ascribed to each plane (Tables 5, and 6).

In addition to the favorable parameterization behavior over the specified distance scale (see Tables 5, and 6), this approach was chosen for a reason which is the significant gap in the returned values of the fit parameters  $\sigma_1 \gg \sigma_2$  signifying the width. In other words, when the transverse profile is fitted using this specific form, the Gaussian distribution

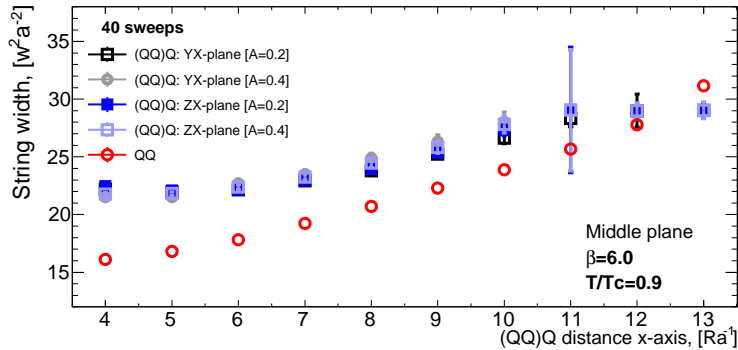


**Figure 18:** Compares the in-plane and perpendicular mean-square width at  $T/T_c = 0.9$  for  $(QQ)Q$  and  $Q\bar{Q}$  systems at the middle plane after  $n_{sw} = 40$  for diquark base of diameter  $A = 2a$ .

function is corrected by another narrower Gaussian but with the same amplitude. That is, the fit function at the centre of the profile is reweighted relative to the tail of the bell-shaped region by the overlap of two Gaussian curves with the same amplitude but different widths.

The action-density shape may be patterned with a heuristic fit-function as shown in Ref. [167], which involves the convolution of a Gaussian distribution appropriate for quantum oscillations with a classical flux-tube profile. The form in Ref. [99] corrects as well the tube's center around the  $Q\bar{Q}$  axis and asymptotically re-weight the tail area. It should be noted that while using the fit ansatz described in the aforementioned literature, we were able to produce good fits at close separation distances but large error bars at farther separations.

The fits to the action density distribution  $\mathcal{C}(r, \theta, x = R/2)$  at the center of the tube Eq.(3.15),  $R/2$ , is shown for diquark-quark separation distances  $R = 0.6, 0.9$  fm and  $R = 1.2$  fm in Figs. 15-16 at the temperatures  $T/T_c = 0.8$  and  $T/T_c = 0.9$ , respectively.

The plots in Figs. 15 and 16 depict the fits for both  $\sigma_1 = \sigma_2$  and  $\sigma_1 \neq \sigma_2$  in Eq.(5.1). Fixing the parameters  $\sigma_1 = \sigma_2$  in the above form Eq. (5.1) corresponds to the standard Gaussian distribution. The best Gaussian fits deviate at the center of the tube as well as the tail region. However, the fits corresponding to the unconstrained form,  $\sigma_1 \neq \sigma_2$ , better fit the center and tail region as discussed above. The fits of this double-Gaussian form return acceptable values of  $\chi^2$  at the intermediate distances  $R$ .

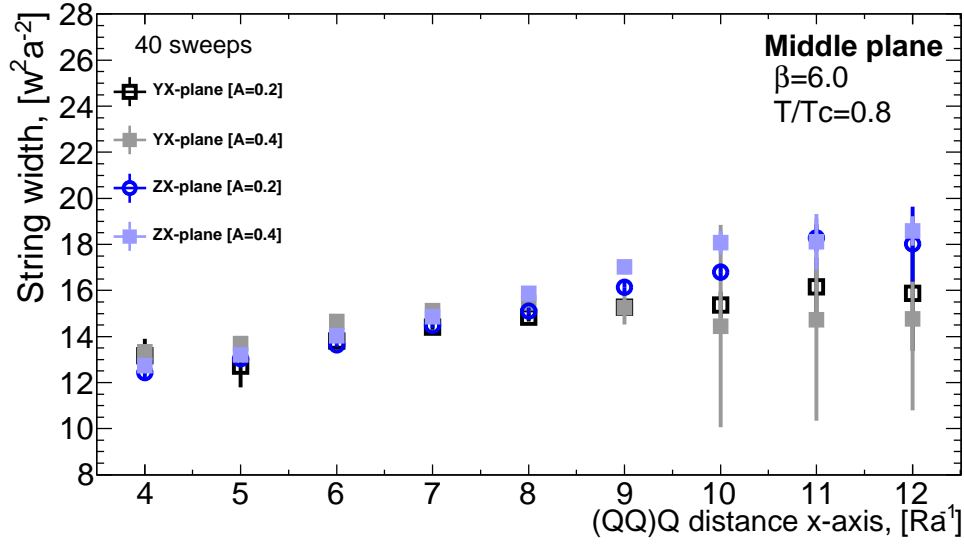
The retrieved parameters from the fit provide a measure of the second moment of the action density distribution with respect to the cylinder's axis  $x$  joining through

$$W^2(x_i) = \frac{\int dr r^3 G(r, \theta; x_i)}{\int dr r G(r, \theta; x_i)}, \quad (5.2)$$

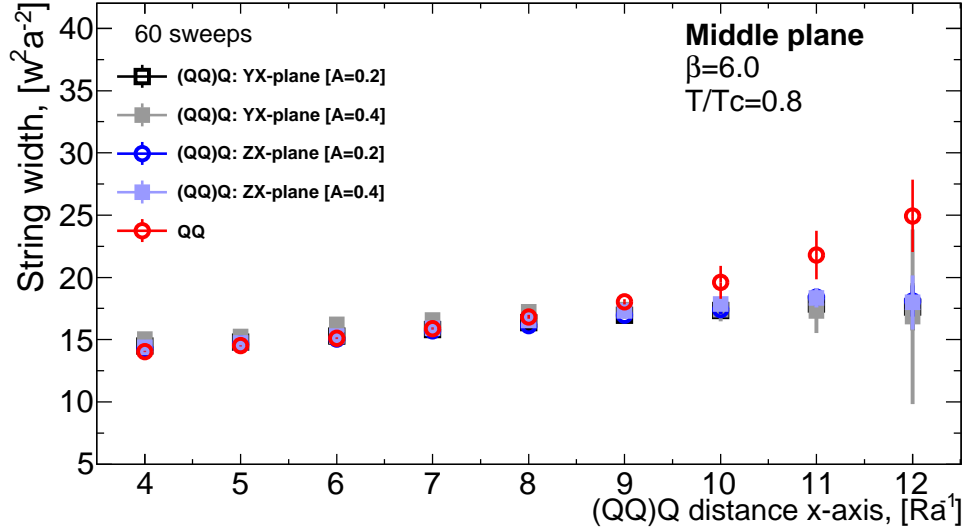
which defines the  $i$ -th data entry of the mean-square width of the tube at the locus  $x_i$  on the lattice. In the case of  $(QQ)Q$  system we measure distinctive values of the width corresponding to in-plane component  $\theta = 0$  and its perpendicular plane  $\theta = \frac{\pi}{2}$ .

The fit parameters of the flux-tube are collected in Table 5 and 6. The width is calculated from the returned values of  $\sigma_1^2$  and  $\sigma_2^2$  through Eq. (5.2).

Inspection of the measured mean-square width (second-moment) discloses that at  $T/T_c = 0.8$ , the mean-square width of the flux tubes of the quark-antiquark and the



(a)



(b)

**Figure 19:** The mean-square width of the string in the middle plane for  $Q\bar{Q}$  and  $(QQ)Q$  of the isosceles base  $A = 0.2, 0.4$  fm “In-plane and perpendicular-plane” at  $T/T_c = 0.8$ .

diquark-quark system are identical within uncertainties of the measurements. However, at the higher temperature  $T/T_c = 0.9$  the measurements of the width reproduce identical values only for long enough flux-tubes  $R \geq 1.0$  fm.

The amplitude profiles in Table. 5 demonstrate, at  $T/T_c = 0.9$ , the similar profile near the quark for each system. Close to the diquark the magnitude of amplitude signifies vacuum expulsions greater than that in the proximity of the antiquark. Nevertheless, the width differences  $\Delta W^2 = W^2(x_i) - W^2(x_j)$  along the flux tube are very small and within the uncertainties of the fit. This contrasts the  $Q\bar{Q}$  width difference at two consecutive planes [41, 51].

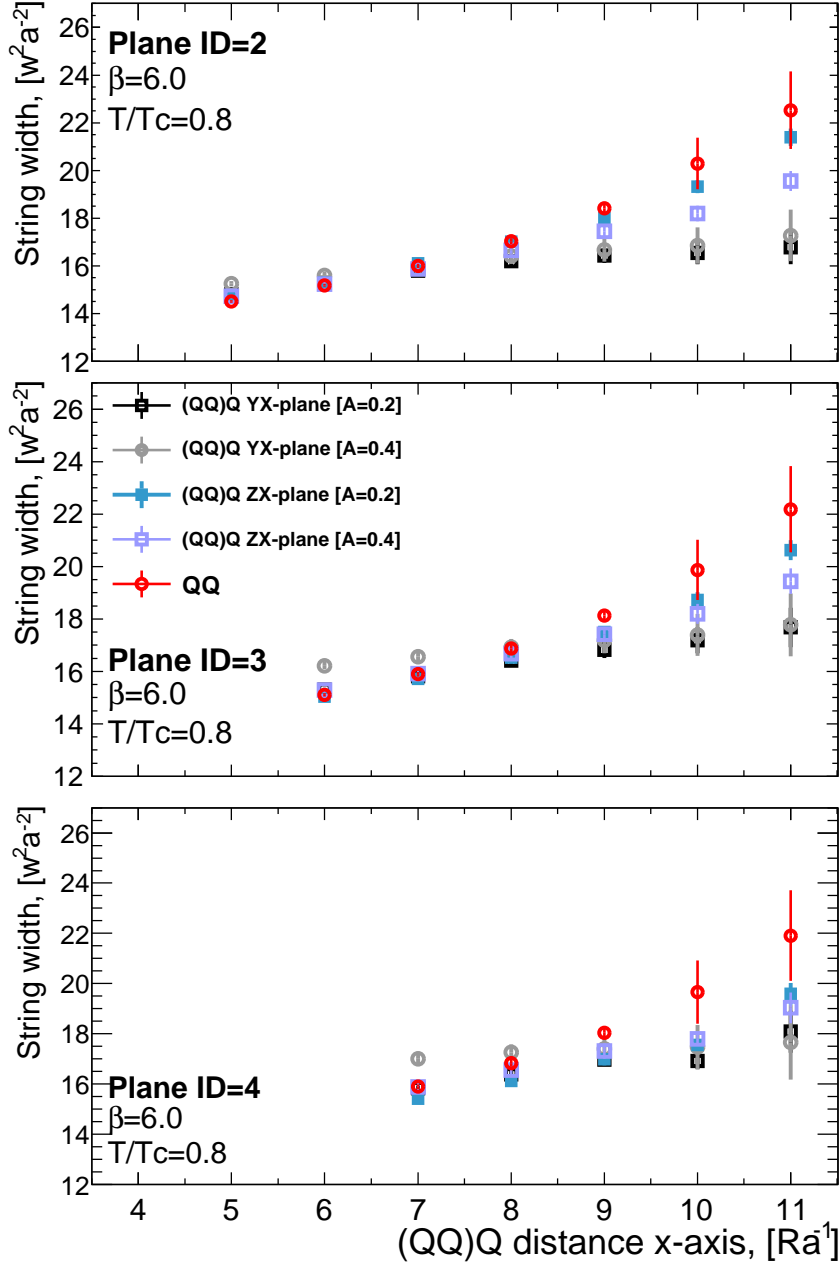


**Figure 20:** The width of the string in the plane,  $z = 2, 3, 4$  for  $Q\bar{Q}$  and  $(QQ)Q$  of the isosceles base  $A = 0.2, 0.4$  fm. In-plane and perpendicular mean-square width at  $T/T_c = 0.8$ .

The values of the mean-square width of the flux-tube at the first four lattice slices from the diquark system are plotted in Fig.17. The width growth is presented at the middle planes  $x = \frac{R}{2}$  and Fig.18. The width corresponding to perpendicular and in-plane fluctuation's of the  $Q(QQ)$  system displays a cylindrical symmetry; even so, the string profile is not identical to that of the  $Q\bar{Q}$  system. The coincidence with the mesonic string does not manifest either at small or intermediate separation regions.

This pinpoints that the string may be energetic enough to induce a splitting towards a

**Table 7:** The returned values of the  $\chi^2(x)$  corresponding to fits of the in-plane width  $W^2(x)$  of the action density at each plane  $x$  to the string model formula Eq.(2.48), the fits are for isosceles triangle quark configuration of base  $A = 2a$  and  $A = 4a$  at  $T/T_c = 0.9$  after  $n_{\text{sw}} = 40$  sweeps.

<b>A = 2a</b>												
Fit range	4-8	4-9	4-10	4-12	5-9	5-10	5-12	6-9	6-10	6-12	7-12	8-12
$\chi^2(1)$	15.7467	27.0586	39.7006	76.2242	5.1557	8.18385	21.888	0.694732	1.73399	9.67608	4.48314	2.1474
$\chi^2(2)$	36.6744	58.1804	78.4037	116.516	10.6706	16.1961	29.815	1.28484	2.48185	7.21768	2.07623	0.781562
$\chi^2(3)$	54.4166	88.878	121.68	172.52	17.6709	27.2391	44.2826	2.41245	4.59691	9.50593	1.80113	0.3457
$\chi^2(4)$					15.16	31.21	49.12	80.01	4.56	9.10	18.51	1.24
<b>A = 4a</b>												
$\chi^2(1)$	16.728	22.3562	28.3737	47.6369	19.3351	22.4557	33.4371	0.216339	0.237681	2.60272	2.44289	1.23397
$\chi^2(2)$	11.9139	18.9942	26.0145	42.4123	3.49132	5.41441	11.7304	0.398579	0.819422	3.296	1.20461	0.541966
$\chi^2(3)$	19.2606	31.8565	43.9118	68.6434	6.7706	10.3598	19.3688	0.897718	1.68898	4.59129	1.12771	0.360786
$\chi^2(4)$					6.21	12.85	19.99	38.56	1.94	3.72	9.82	0.46

**Table 8:** Same as Table 7. However the values of the  $\chi^2$  are returned from the fits of formula Eq.(2.47) to the perpendicular width of the action density  $W^2(x)$  and  $n_{\text{sw}} = 40$  sweeps.

<b>A = 2a</b>												
Fit range	4-8	4-9	4-10	4-12	5-9	5-10	5-12	6-9	6-10	6-12	7-12	8-12
$\chi^2(1)$	43.6488	70.643	95.8211	139.296	14.0156	21.01	35.5021	1.76644	3.20865	7.46718	1.55846	0.451334
$\chi^2(2)$	52.935	89.9815	125.779	182.096	19.3283	29.9856	48.5269	2.85559	5.28193	10.3058	1.68293	0.254988
$\chi^2(3)$	65.7849	113.944	163.981	244.385	24.7828	40.5754	68.2562	3.94029	7.97634	15.9491	2.90368	0.363801
$\chi^2(4)$					16.59	35.86	59.61	105.76	5.62	12.072694	11.88	1.56
<b>A = 4a</b>												
$\chi^2(1)$	17.0601	27.9284	38.6724	59.6416	5.46255	8.43977	15.7773	0.670376	1.3058	3.72269	0.997622	0.352228
$\chi^2(2)$	20.45	34.4918	48.0338	70.617	7.53652	11.5326	19.0597	1.02559	1.8569	3.85362	0.650788	0.134616
$\chi^2(3)$	25.7955	44.7738	63.8724	94.1709	10.0837	15.9441	25.8421	1.51211	2.86368	5.38821	0.806941	0.083399
$\chi^2(4)$					6.82	14.71	23.92	40.32	2.32	4.71	9.50	0.65

**Table 9:** The returned values of the  $\chi^2(x)$  corresponding to fits of the in-plane width  $W^2(x)$  to the mesonic string formula given by Eq.(2.40) at the corresponding plane  $x$ , the fits are for isosceles triangle quark configuration of base  $A = 2a$  and  $A = 4a$  at  $T/T_c = 0.9$ .

<b>A = 2a</b>								
Fit range	4-9	5-10	4-12	5-12	6-12	7-12	8-12	
$\chi^2(1)$	29.9	46.6	99.6	99.4	91.3	57.3	32.1	
$\chi^2(2)$	65.0	91.7	156.7	155.5	120.3	69.6	33.5	
$\chi^2(3)$	93.3	117.4	203.0	193.5	156.0	91.2	41.9	
$\chi^2(4)$	–	122.38	–	215.3	195.3	123.9	59.9	
<b>A = 4a</b>								
$\chi^2(1)$	23.1	30.8	58.5	56.8	56.8	21.9	13.1	
$\chi^2(2)$	26.2	38.4	69.26	66.7	47.6	27.0	13.5	
$\chi^2(3)$	33.6	50.7	88.40	88.3	67.3	38.9	18.6	
$\chi^2(4)$	–	52.4	–	105.6	92.8	59.6	30.2	

baryonic-like structure [39, 40]. Indeed we have found in the previous section a significant change in the numerical values of the Polyakov correlators of  $(QQ)Q$  system for  $R < 1$  fm with the increase of the temperature as depicted in the potential plot of Fig. 7(b). In the next section, we assess the width-growth pattern in the light of bosonic string models for either mesonic and baryonic arrangements.

**Table 10:** The returned values of the  $\chi^2(x)$  corresponding to fits of the in-plane width  $W^2(x)$  of the action density at each plane  $x$  to the string model formula Eq.(2.48), the fits are for isosceles triangle quark configuration of base  $A = 2a$  and  $A = 4a$  at  $T/T_c = 0.8$ ,  $n_{sw} = 60$  sweeps.

baryon:		A = 2a							A = 4a						
Fit range	4-8	4-9	4-10	5-10	4-12	5-12	6-12	4-8	4-9	4-10	5-9	4-12	5-12	6-12	
$\chi^2(1)$	3.10	1.60	1.61	6.98	13.90	7.00	1.93	0.83	1.02	1.10	1.02	1.18	1.18	0.51	
$\chi^2(2)$	4.12	4.89	5.20	0.39	5.65	0.45	7.17	1.60	2.04	2.29	1.86	2.93	2.82	1.73	
$\chi^2(3)$	9.51	11.33	12.5	1.92	14.43	2.61	0.40	2.81	3.31	3.63	2.35	4.31	3.48	1.84	
$\chi^2(4)$	-	-	-	2.10	-	3.09	0.71	-	-	-	-	1.37	1.41	0.25	
meson:		A = 2a							A = 4a						
Fit range	4-8	5-8	6-9	4-12	5-12	6-12	7-12	4-8	5-8	6-9	4-12	5-12	6-12	7-12	
$\chi^2(1)$	2.1	1.96	0.83	2.33	2.20	0.87	0.19	0.68	0.75	0.55	0.79	0.58	0.30	0.30	
$\chi^2(2)$	58.26	1.14	0.22	58.76	1.22	6.15	1.15	202.31	16.7	1.98	218.47	20.05	2.46	0.40	
$\chi^2(3)$	1215.1	97.31	6.98	1249.5	103.93	16.99	7.40	2520.96	243.0	31.7	2679.5	295.1	39.17	7.13	
$\chi^2(4)$	-	640.11	84.68	-	698.68	87.03	8.85	-	737.8	144.1	-	827.7	162.95	14.53	

Near the end of QCD plateau, see Fig.12,  $T/T_c = 0.8$ , we find the mean-square width of the energy profiles of  $(QQ)Q$  to be very similar considering the middle plane as depicted in Fig. 19. The same assertion on the broadening of the profile at planes other than the middle, see Fig.20, holds as well. In the vicinity of the quark, the action density exhibits cylindrical symmetry even for  $3Q$  arrangement with base length  $A = 0.4$  fm.

It's compelling to emphasize that neither the observed symmetry nor asymmetry between the two systems is significantly impacted by the number of UV filtering sweeps,  $n_{sw}$ . On Fig. 19 we show results of measurements made at the intermediate planes while taking into account two cooling levels.

The findings from the analysis in this section concur with that of the Polyakov loop correlators in the preceding section. In addition, we stress the close analogy between the analysis at the end of the QCD Plateau [39, 40], and that utilizing the Wilson-loop overlap formalism [143] or three Polyakov-loops [142] at  $T = 0$ .

## 5.2 Broadening of effective strings

The numerical values of the mean-square width (Table 5 and 6) indicate a broadening in mean-square width of the string at all transverse planes  $x_i$  as the color sources have pulled a distance  $R_i$  apart (Fig. 17-20).

This section's goal is to reveal the nature of the flux tube's widening. This is another instance of the suitability of bosonic string models to investigate the growth behavior with the increase of color source separation. The mean-square width is opposed with the equivalent string model equations in Eq. (2.47), Eq.(2.48) and Eq.(2.40) for both mesonic and baryonic strings, respectively.

The fits are obtained by the parameter space  $R_0$  in the above-mentioned models such that the least square residuals

$$\chi^2(R = x_j; R_0) = \sum_i \left( \frac{(W_i^2(R) - W_{model}^2(R; R_0))}{e_i(R)} \right)^2, \quad (5.3)$$

are minimized. In the above equation (5.3),  $e_i^2(R_i)$  is the square of the error in the measured mean-square width  $W_i^2(R_i)$  from the lattice simulation (5.2).

Here, the analysis of the fit behavior of the mean-square width data is discussed keeping the string tension fixed to the standard value returned from the lattice simulations at zero temperature  $\sigma a^2 = 0.044$  [142].

As the third quark  $Q_3$  is being dragged distances  $R$  apart from the triangle's base, we concentrate on analyzing the fit behavior at the first four subsequent planes near the diquark  $x_i = 1, 2, 3, 4$ . This should show whether there are fairly substantial signatures of the baryonic junction on the broadening profile at the relevant quark configuration.

It is standard to set the geometrical form of the Y-string configuration of the model itself prior to the fit to the action density data. The intersection point is placed at the Steiner point, where the total length of the three strings is at its shortest. The junction at Fermat point  $x_f$  of the isosceles triangular configuration is seen in the classical solution of the Y-string configuration in Fig. 6. The analysis of a baryonic junction on a lattice structure may be greatly simplified with the use of this planar quark configuration since the Fermat point's location only depends on the base length, which is kept fixed while the third quark's position  $R$  varies with the Fermat point's locus.

We engage in the flux tube's action density of the  $3Q$  planar configuration corresponding to isosceles triangles, but with the  $(QQ)Q$  bases of length  $A = 2a$ ,  $A = 4a$  only being taken into account. This is analogous to our analysis regarding the confining force in the previous section.

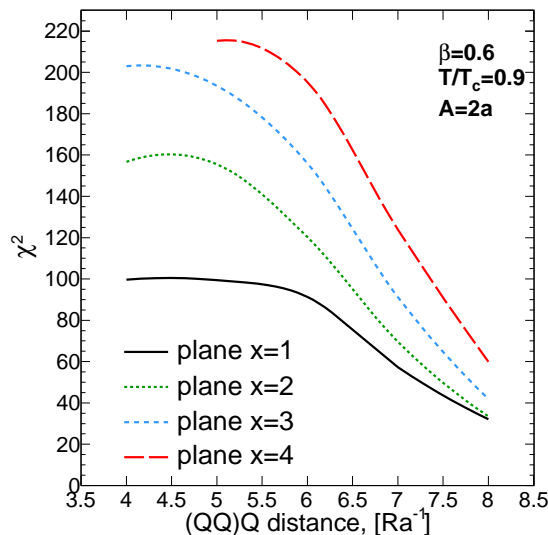


**Figure 21:** The returned  $\chi^2$  for fits to the mesonic string model for the in-plane fluctuations Eq.(2.40) at the first four planes at  $T/T_c = 0.9$ .

The two components of the width at the first four transverse planes,  $x = 1$  to  $x = 4$ , are provided in Tables 5 and 6. The measurements are enlisted versus the third color source  $Q_3$  separation  $R$ , also see Figs. 17, 18, 19 and 20.

The Y-string implies perpendicular and in-plane mean-square width of the junction fluctuations given by Eq.(2.47) and Eq.(2.48), respectively. Since the junction's oscillations are not projected to smooth out and will likely produce a local peak, the fit behavior ought

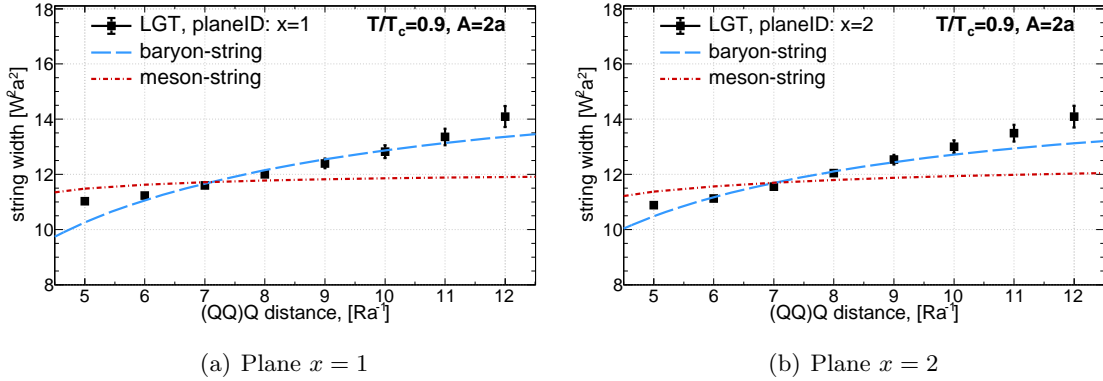


**Figure 22:** The data corresponds to the mean-square width of the action density in the  $3Q$  plane at  $T/T_c = 0.9$  at plane  $x = 1$  from the diquark, the lines are the fit of baryonic string Eq.(2.48) for the in-plane fluctuation of the junction and mesonic string Eq.(2.40).

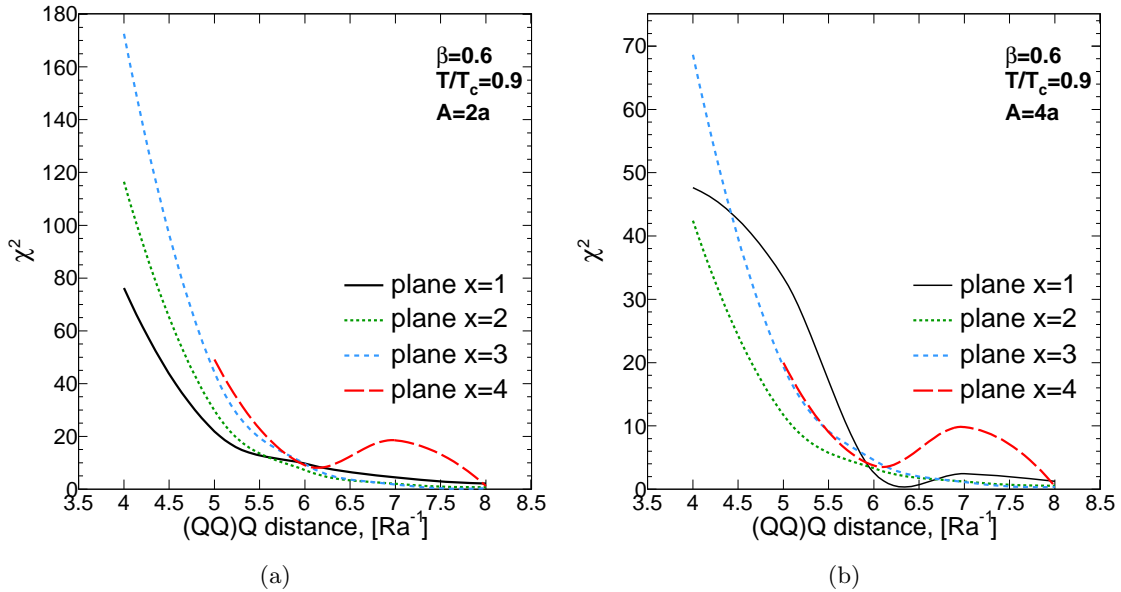


**Figure 23:** The returned  $\chi^2$  for fits to the baryonic string model for the in-plane fluctuations Eq.(2.48) at the first four planes. (a) Diquark base  $A = 2a$  and (b) Base  $A = 4a$ .

to be examined at each selected transverse plane to the tube's measured widths.

At the highest temperature  $T/T_c = 0.9$ , Table 7 and Table 8 summarize the returned values of  $\chi^2(x_i)$  from resultant fits to the two width components (in-plane and perpendicular plane Table 5) for the indicated separation range  $R \in [a, b]$  at four consecutive transverse planes  $x = 1$  to  $x = 4$ .

In general, the fits in Table 7 and Table 8 show strong dependency on the fit range with high values of  $\chi^2(x_i)$  when including points at small  $Q_3$  source separations or long fit intervals. However, the values of  $\chi^2(x_i)$  rapidly decrease when excluding those points at short distance separations.

With large values of  $\chi^2(x_i)$  when including points at short  $Q_3$  source separations or

lengthy fit intervals, the fits in Table 7 and Table 8 generally exhibit substantial dependence on the fit range. When those points with close distances separating the  $Q_3$  source are excluded, the residuals  $\chi^2(x_i)$  values, however, rapidly decline.

Nevertheless, it is clear that the best fits are for planes  $x = 1$  and  $x = 2$ , which are one to two lattice spacings from the base. In Ref. [39], where we performed a comparative analysis with a high base length, it was noted that the corresponding  $\chi^2(x_i)$  is minimized at planes closer to the junction's mean location. That is, certain planes may display higher contributions received from the fluctuations in the vicinity of the junction.

The length of the base of the triangular isosceles quark configuration affects the plane at which we attain the minimum in  $\chi^2(x_i)$ . The two strings of the Y form are closer together in space when the base is narrow, and self-interactions can result in more conspicuous deviations. This argues that when the system approaches the typical baryonic configuration, the junction effects become more significant. One, accordingly, can observe

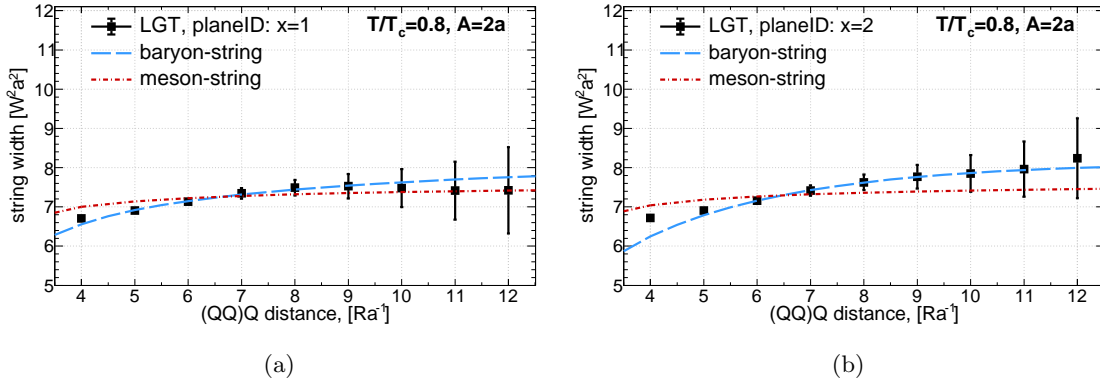


**Figure 24:** Same as Fig.22. However, the data and fits of mean-square width are taken at temperature  $T/T_c = 0.8$ .

that the increase of the base length results in a reduction of the residuals which can be seen by examining the values corresponding to the configurations with  $A = 2a$  and  $A = 4a$  in Tables 7 and 8. The plots of  $\chi^2(x_i)$  for selected fit regions at planes  $x = 1$  to  $x = 4$  are displayed in Fig. 23.

Similar to our arguments regarding the  $3Q$  potential in the previous section, we would like to assess the mesonic-like aspects of the width of the fluctuations at  $T/T_c = 0.9$ . The mean-square width of the meson Eq. (2.40) is fit to the baryonic flux-tube width Tables 7 and 8.

Table 9 summarizes the returned  $\chi^2(x_i)$  from the fits to the mesonic string mean-square width given by Eq.(2.40) to the in-plane fluctuations  $W^2(x_i)$  of the diquark-quark  $(QQ)Q$  enlisted in Table 5. The fits return higher values of the residuals  $\chi^2(x_i)$  compared to the corresponding fits for baryonic string Tables 7, Table 8. This can readily be seen by inspecting Fig. 21 which shows significantly higher values of  $\chi^2(x_i)$  at the first four considered planes.

At the same temperature  $T/T_c = 0.9$ , both fits for the baryonic string Eq.(2.48) and mesonic string Eq.(2.40) are plotted in Fig.22. The fitting range is given by  $R \in [6a, 11a]$ .

Unexpectedly, the  $Q\bar{Q}$  mesonic string and the lattice data for the diquark-quark  $(QQ)Q$  configuration  $A = 2a$  do not correspond well. This supports the potential that junction interactions ensue in this temperature.

Fig. 23 displays the change in the residuals at the first four planes from the diquark. The  $\chi^2(x_i)$  minima do occur at the planes  $x = 1$  and  $x = 2$ , which are near to the Fermat point of the configuration. In fact, the occurrence of certain planes at which the lattice data best agrees with the baryonic Y-string formulated of Eq.(2.47) and Eq.(2.48) suggests that the junction impacts would manifest at temperatures as high as  $T/T_c = 0.9$ . The effects of the junction eventually fade away at distant planes from the diquark.

On the other hand, at the lower temperature  $T/T_c = 0.8$  we enlisted in Table 10 the returned  $\chi^2(x_i)$  from the fits to the in-plane fluctuations  $W^2(x_i)$  of the diquark-quark. The two panels in the table compare the fits for both the mesonic and baryonic strings given by Eq.(2.40) and Eq.(2.48), respectively.

The fits return good values of  $\chi^2(x_i)$  at the first four considered planes compared to the corresponding fits for baryonic string Tables.7. This is reflected in the plots of Fig. 24 which compare the resultant fits of both strings at temperature  $T/T_c = 0.8$ . The diminish of the deviations (Fig. 22) of the lattice data from the mesonic string's width profile is palpable.

The Y-string model at the depicted planes  $x = 1$  and  $x = 2$  the in-plane fluctuations of the diquark-quark flux-tube return good  $\chi^2(x_i)$  base lengths  $A = 2a$  (see Fig.24). The diquark-quark and  $Q\bar{Q}$  similarity manifest obviously. This points to the subtle effects of the junction as the Y-string approaches the limit of its mesonic counterpart at this temperature.

In summary, the mean-square width of the  $(QQ)Q$  gluonic energy density and its broadening pattern reveal comparable profile to the  $Q\bar{Q}$  systems. The coincidence is observed up to temperatures near the end of QCD Plateau. However, when close enough to the critical point the diquark-quark and the quark-antiquark expose variant profiles. The gluonic energy-density do exhibit baryonic-like characteristics for quark source separations in the intermediate distance scales. The width of the gluonic modes of the  $(QQ)Q$  shows clear deviation from the mesonic string but compares well with that from the Y-bosonic string model.

The mesonic limit of diquark-quark baryon can be a good approximation for low-lying states. This has been observed considering the lattice parameters presented here and in Refs [142, 143]. The propagation in the Euclidean time of the Wilson loop together with the APE link-blocking in Ref. [143] have been sufficient for the excited decuplet baryonic states to decay yielding an optimal overlap with the mesonic ground state. However, with the rise of the temperature overlaps with higher-order states do occur. The excited baryonic states cause splitting from the meson-like behavior.

To establish the scale dependence of the systems under scrutiny, a careful analysis considering smaller lattice spacings, smaller neighborhoods of  $T_c$ , higher states of excited spectrum [89, 168, 169] and even strong magnetic fields [170–174] ought to be addressed.

## 6. Conclusion and prospect

In this work, we inspect the symmetry between the gluon flux tubes for the quark-antiquark  $Q\bar{Q}$  and three quark systems at finite temperature. We approximate the baryonic quark-diquark  $(QQ)Q$  configuration by constructing the two quarks at a small separation distance of at least 0.2 fm.

The potential and energy-density characteristics of the  $Q\bar{Q}$  and  $(QQ)Q$  systems are examined. Both the Polyakov loop and the action-density correlator provide the same almost identical structure up to temperatures near the end of the QCD Plateau. However, when the temperature gets close to the deconfinement point, the symmetry between the two systems breakdown. The gluonic characteristics display splitting for quark source separations  $R < 1.0$  fm.

The numerical data of the  $(QQ)Q$  potential are investigated in light of the fits of mesonic and baryonic string models. The baryonic string model approaches the free mesonic string reproducing the same value for the string tension. However, near the crucial point  $T/T_c = 0.9$ , in contrast to the free mesonic string the Y-baryonic string model's fit of the potential yields a decent  $\chi^2$  value with a string tension value same as the corresponding  $Q\bar{Q}$  arrangement.

Similarly, the analysis of the mean-square width of the energy profile indicates baryonic-like aspects consistent with the Goldstone modes of Y-bosonic string at  $T/T_c = 0.9$  at all considered transverse planes. The mesonic string profile displays large deviations from the diquark-quark data at planes close to the diquark system. At the lower temperature, the  $(QQ)Q$  baryon displays a broadening profile consistent with both mesonic and Y-string models with the same string tension as the quark-antiquark  $Q\bar{Q}$  system.

These findings limit the validity that, in the quenched approximation, the  $(QQ)Q$  precisely share many properties in common with the  $Q\bar{Q}$  to the Plateau region of QCD [142, 143]; otherwise, excited baryonic states can manifest around small neighborhoods of the QCD critical point signaling a cross over into the junction behavior.

It would be intriguing to perform the computations afterward while using smaller lattices and taking greater temperatures or dynamical quarks into consideration. It is justifiable that the meson-baryon symmetry would be questioned in the context of an excited spectrum, or in the presence of strong magnetic fields. Future work ought to probe these arrangements, which are likely to be of substantial importance to phenomenological models of hadron structure.

## Acknowledgments

The authors thank the Yukawa Institute for Theoretical Physics, Kyoto University. Discussions during the YITP workshop YITP-T-14-03 on “Hadrons and Hadron Interactions in QCD” were useful in completing this work. We thank Philippe de Forcrand for suggesting the investigation of the mesonic aspects of the  $(3Q)$  systems. This work has been funded by the Chinese Academy of Sciences President's International Fellowship Initiative grants No.2015PM062 and No.2016PM043, the Recruitment Program of Foreign Experts,

NSFC grants (Nos. 11035006, 11175215, 11175220) and the Hundred Talent Program of the Chinese Academy of Sciences (Y101020BR0).

## A. Appendix A

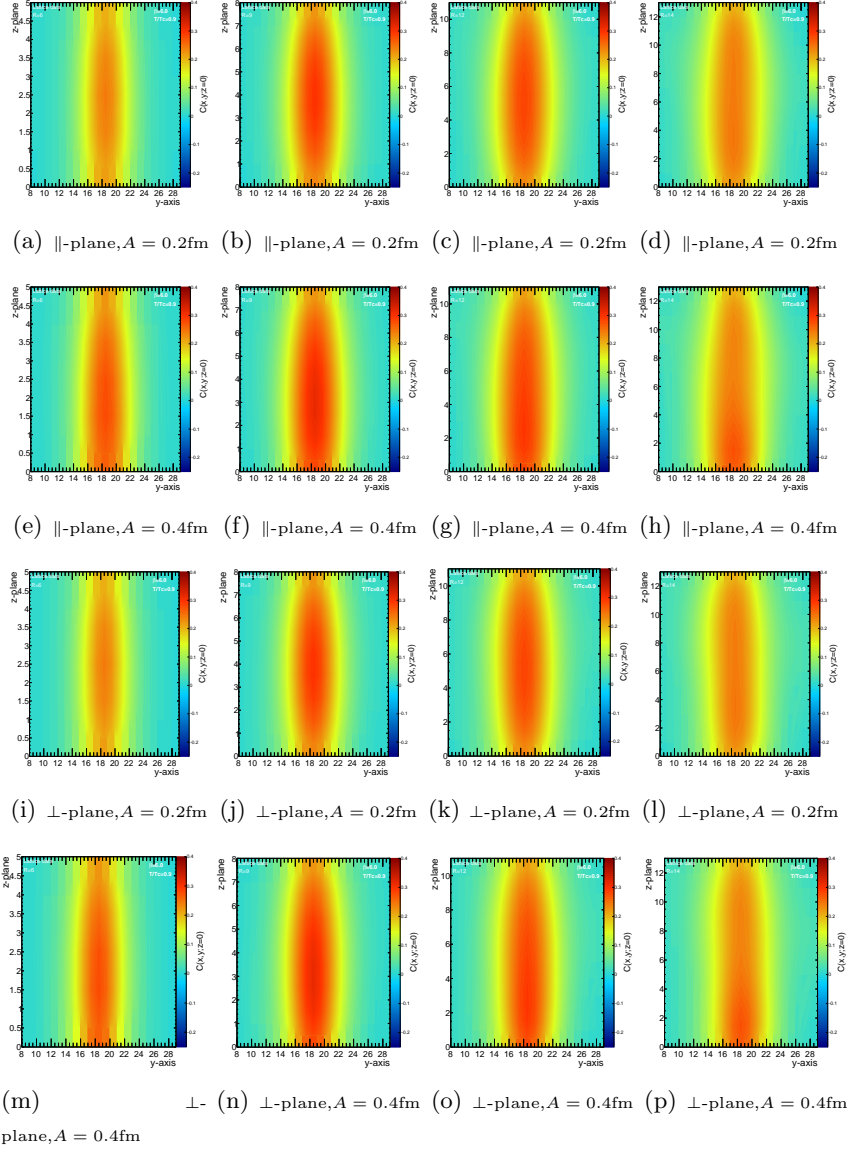


**Figure 25:** Flux tubes in 2D-plane for source separations  $R = 0.6, 0.9, 1.2, 1.4$  fm (from top to bottom) and temperature  $T/T_c \approx 0.9$ . Panels on the top correspond to the quark-diquark system (baryon), panels on the very bottom – to the quark-antiquark system (meson). For the baryon system the flux tube is shown in two projection planes  $yz$ (a–h) and  $xz$ (i–p), and for the two values of the distance between  $Q_1$  and  $Q_2$  quarks  $A = 0.2, 0.4$  fm, see Fig.4 for details.

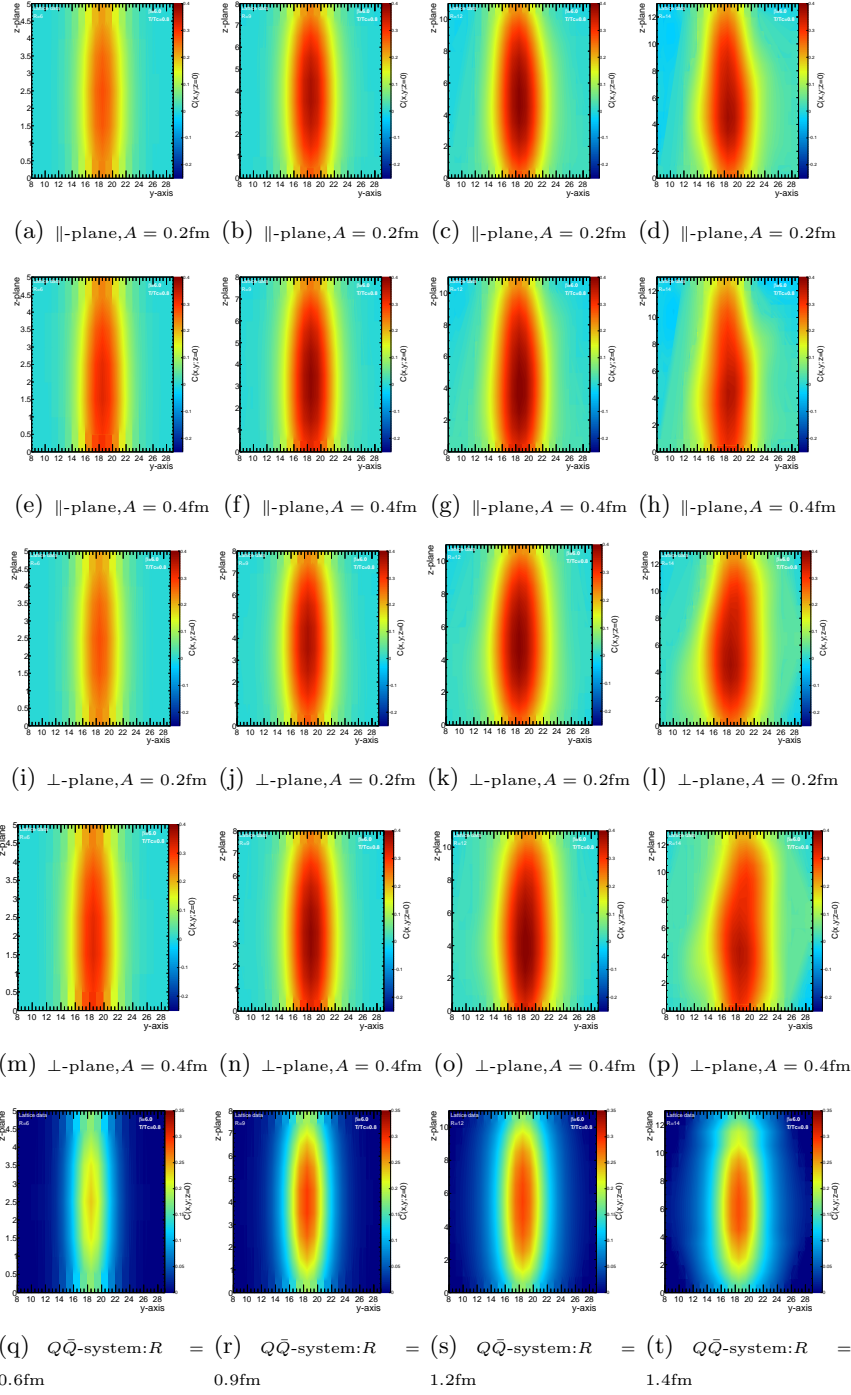


**Figure 26:** Flux tubes in 2D-plane for source separations  $R = 0.6, 0.9, 1.2, 1.4$  fm (from top to bottom) and temperature  $T/T_c \approx 0.8$ . Panels on the top correspond to the quark-diquark system (baryon), panels on the very bottom – to the quark-antiquark system (meson).

## References

- [1] M. Gell-Mann, *A Schematic Model of Baryons and Mesons*, Phys. Lett. **8** (1964), 214–215.

- [2] M. Ida, R. Kobayashi, *Baryon resonances in a quark model*, Prog. Theor. Phys. **36** , 846 (1966)
- [3] D.B. Lichtenberg, L.J. Tassie, *Baryon Mass Splitting in a Boson-Fermion Model*, Phys. Rev. **155**, 1601–1606 (1967)
- [4] D.B. Lichtenberg, L.J. Tassie, P.J. Keleman, *Quark-Diquark Model of Baryons and SU(6)*, Phys. Rev. **167**, 1535–1542 (1968)
- [5] J. Carroll, D.B. Lichtenberg, J. Franklin, *Electromagnetic properties of baryons in a quark-diquark model with broken SU(6)*, Phys. Rev. **174**, 1681-1688 (1968)
- [6] S. Ono, *A two-body baryon model*, Prog. Theor. Phys. **48**, 964–973 (1972)
- [7] V.V. Anisovich, *Coherent Interaction of Leptons with Quarks in Deep Inelastic Processes*, Pis'ma ZhETF21, 382 (1975) [JETP Lett.21, 174 (1975)]
- [8] V.V. Anisovich, P.E. Volkovitsky, V.I. Povzun, *Description of Deep Inelastic Processes in the Composite Quark Model*, ZhETF 70, 1613 (1976) [Sov.Phys. JETP 43, 841 (1976)]
- [9] I.A. Schmidt, R. Blankenbecler, *Nonscaling for Everyman: The Proton, Neutron and Deuteron Structure Functions*, Phys. Rev. **D16**, 1318 (1977)
- [10] M. Anselmino, E. Predazzi, *Diquarks*. Proceedings, Workshop, Turin, Italy, October 24-26, 1988, (Singapore: World Scientific (1989) 297 p)
- [11] M. Anselmino, E. Predazzi, S. Ekelin, S. Fredriksson, D.B. Lichtenberg, *Diquarks*, Rev. Mod. Phys. **65**, 1199–1234 (1993).
- [12] M. Anselmino, E. Predazzi, *Diquarks*. Proceedings, 2nd Workshop, Villa Gualino, Turin, Italy, November 2-4, 1992 (Singapore: World Scientific (1994) 291 p)
- [13] K. Goeke, P. Kroll, H.R. Petry, *Quark cluster dynamics*. Proceedings, 99th WE Heraeus Seminar, Bad Honnef, Germany, June 29-July 1, 1992 Lect. Notes Phys. 417 (1993)
- [14] Koji Hashimoto, *Nuclear Force from String Theory*, Nucl. Phys. **A 835-1**, 192-198 (2010), Proceedings of the 10th International Conference on Hypernuclear and Strange Particle Physics,
- [15] Y. Nambu, Phys. Rev. **D10**, 4262, 310(1974)
- [16] Y. Nambu, Phys. Lett. **B 80**, 372 (1979)
- [17] Y. Nambu, Proc. Int. Conf. Symmetry and quark models, Wayne State U. 1969; T.Goto, *Relativistic quantum mechanics of one-dimensional mechanical continuum and subsidiary condition of dual resonance model*, Prog.Theor.Phys.**46**, 1560-1569 (1971),

- H. Nielsen, Report at the 15th Int. Conf. on High-energy Physics (Kiev)  
 L. Susskind, *Dual symmetric theory of hadrons. 1*, Nuovo Cim.**69**, 457-496 (1970),
- [18] A.P. Balachandran *et al.*, *Strings, Monopoles and Meson States*, Phys. Rev. **D13**, 361 (1976)
- [19] G.'t Hooft, *A Planar Diagram Theory for Strong Interactions*, Nucl. Phys. **B72**, 461 (1974)
- [20] I. Bars, A.J. Hanson, *Quarks at the Ends of the String*, Phys. Rev. **D13**, 1744-1760 (1976).
- [21] R. Giles, S.H.H. Tye, *Quantum Dynamics of a Quark Binding Bubble in Two Space One Time Dimensions*, Phys. Rev. **D13**, 1690 (1976).
- [22] Jr. Callan, G. Curtis, N. Coote, D.J. Gross, *Two-Dimensional Yang-Mills Theory: A Model of Quark Confinement*, Phys. Rev. **D13**, 1649 (1976)
- [23] R. Andreo, F. Rohrlich, *A string model of mesons*, Nucl. Phys. **B115**, 521–532 (1976)
- [24] O. Andreev, *Some Aspects of Three-Quark Potentials*, Phys. Rev. **D93** (2016) no.10, 105014 [arXiv:1511.03484 [hep-ph]].
- [25] L.D. Solovev, *Masses and internal structure of mesons in the string quark model*, Phys. Rev. **D61**, 015009 (2000) [arXiv:hep-ph/9907486]
- [26] O. Jahn, Ph. de Forcrand, Lattice field theory. Proceedings, 21st International Symposium, LATTICE2003, Tsukuba, Japan, July 15-19, 2003 Nucl. Phys. Proc. Suppl. **129**, 700-702 (2004) [arXiv:hep-lat/0309115]
- [27] Ph. de Forcrand, O. Jahn, *The Baryon static potential from lattice QCD*. [The structure of baryons. Proceedings, 10th International Conference, Baryons'04, Palaiseau, France, October 25-29, 2004] Nucl. Phys. **A755**, 475-480 (2005) [arXiv:hep-ph/0502039]
- [28] M. Pfeuffer, G. S. Bali, M. Panero, Phys. Rev. **D79**, 025022 (2009) [arXiv:0810.1649]
- [29] Z. Liu, T. DeGrand, *Baryon correlators containing different diquarks from lattice simulations*. Proc. Science LAT2006 116 (2006) [arXiv:hep-lat/0609038].
- [30] M. Hess, F. Karsch, E. Laermann, I. Wetzorke *Diquark masses from lattice QCD*. Phys. Rev. **D58**, 111502 (1998) [arXiv:hep-lat/9804023].
- [31] R. Babich *et al.* *Light hadron and diquark spectroscopy in quenched QCD with overlap quarks on a large lattice*. JHEP **0601** 096 (2006) [arXiv:hep-lat/0509027].
- [32] K. Orginos *Diquark properties from lattice QCD*, Proc. Science LAT2005, 054 (2006) [arXiv:hep-lat/0510092].

- [33] C. Alexandrou, Ph. de Forcrand, B. Lucini, *Evidence for diquarks in lattice QCD*, Phys. Rev. Lett. **97**, 222002 (2006) [arXiv:hep-lat/0609004].
- [34] R. Babich *et al.*, *Diquark correlations in baryons on the lattice with overlap quarks*. [arXiv:hep-lat/0701023].
- [35] M. Cardoso, P. Bicudo, N. Cardoso, *Detailed study of quark-antiquark flux tubes and flux tube recombination* [Proceedings, 4th Workshop on Excited QCD 2012: Peniche, Portugal, May 6-12, 2012], Acta Phys.Polon.Supp. Vol.5, 1149–1154 (2012) [arXiv:hep-lat/1208.2552].
- [36] D. Giataganas, K. Goldstein, *Tension of Confining Strings at Low Temperature*, JHEP **02** (2015), 123 [arXiv:1411.4995 [hep-th]].
- [37] P. Bicudo, M. Cardoso, N. Cardoso, *SU(3) quark-antiquark QCD flux tube*. [Proceedings, 31st International Symposium on Lattice Field Theory (LATTICE2013): Mainz, Germany, July 29-August 3, 2013] PoS. **LATTICE2013**, 495 (2014) [arXiv:hep-lat/1401.6008].
- [38] A.S. Bakry, X. Chen, P.M. Zhang, *The confining baryonic Y-strings on the lattice*, Proceedings, 11th Conference on Quark Confinement and the Hadron Spectrum (Confinement XI): St. Petersburg, Russia, September 8-12, 2014. AIP Conf. Proc. 1701, 030001 (2016), [arXiv:hep-lat/1412.3568].
- [39] A. Bakry, X. Chen, P.-M. Zhang, *Y-stringlike behavior of a static baryon at finite temperature*. Phys. Rev. **D91** (2015) 114506 [arXiv:hep-lat/1412.3568].
- [40] A.S. Bakry, X. Chen, P.-M. Zhang *Confining potential of Y-string on the lattice at finite T*, Proceedings, 4th International Conference on New Frontiers in Physics (IC-NFP 2015): Crete, Greece, August 23-30, (2015), EPJ Web Conf. **126** (2016) 05001, <http://arxiv.org/abs/1706.01255> .
- [41] A. Bakry, M. Deliyergiyev, A. Galal, A. Khalaf, M. Khalil, *Quantum delocalization of strings with boundary action in Yang-Mills theory*, <http://arxiv.org/abs/2001.02392>, M. Khalil et. al, *boundary corrections of LW string action* , Talk given at Virtual Tribute to Quark Confinement and the Hadron Spectrum 2021, Aug (2021).
- [42] A. Bakry, M. Deliyergiyev, A. Galal, M. Khalil, *Boundary action and profile of effective bosonic strings*, <http://arxiv.org/abs/1912.13381>, M. Khalil, A. Bakry, X. Chen, M. Deliyergiyev, A. Galal, A. Khalaf, P .M Zhang, *On boundary corrections of Lüscher-Weisz string*, EPJ Web Conf. **258** (2022) 02004, <https://doi.org/10.1051/epjconf/202225802004>
- [43] A.S. Bakry, X. Chen, M.A. Deliyergiyev, A. Galal, A. Khalaf, P.M. Zhang, *Stiff self-interacting strings at high temperature QCD*, EPJ Web Conf. **175** (2018) 12004. <https://doi.org/10.1051/epjconf/201817512004>

- [44] A.S. Bakry, X. Chen, M.A. Deliyergiyev, A. Galal, S. Xu, P.M. Zhang, *Mesonic String of Diquark-Quark Configuration at Finite Temperature*, PoS **HADRON2017** (2018) 211. <https://arxiv.org/abs/1712.03109>
- [45] A.S. Bakry, M.A. Deliyergiyev, A.A. Galal, M.N. Khalil, *Perturbative width of open rigid strings*, Phys.Rev. **D105** (2022) 094504. <https://arxiv.org/abs/1709.09446>
- [46] A.S. Bakry, Xurong Chen, Pengming Zhang, *Noise reduction by combining smearing with multi-level integration methods*, Int. J. Mod. Phys. **E23** (2014) 1460008.
- [47] A.S. Bakry, D.B. Leinweber, B. Derek, A.G. Williams, *Gluonic fields as unraveled with Polyakov lines and predicted by bosonic strings*, PoS **LATTICE2012** (2012) 271.
- [48] A.S. Bakry, D.B. Leinweber, B. Derek, A.G. Williams, *On the ground state of Yang-Mills theory*, Annals Phys. **326** (2011) 2165–2173. <https://arxiv.org/abs/1102.3477>
- [49] A.S. Bakry, D.B. Leinweber, B. Derek, A.G. Williams, *Gluonic profile of static baryon at finite temperature and the Y baryonic string*, PoS **LATTICE2011** (2011) 256.
- [50] A.S. Bakry, D.B. Leinweber, A.G. Williams, *Bosonic stringlike behavior and the Ultraviolet filtering of QCD*, Phys.Rev. **D85** (2012) 034504. <http://arxiv.org/abs/1011.1380>
- [51] A.S. Bakry, D.B. Leinweber, P.J. Moran, A. Sternbeck, A.G. Williams, *String effects and the distribution of the glue in mesons at finite temperature*, Phys.Rev. **D82** (2010) 094503. <https://arxiv.org/abs/1004.0782>
- [52] A.S. Bakry, D.B. Leinweber, A. G.Williams, *Gluonic profile of the static baryon at finite temperature*, Phys. Rev. **D91** (2015) 094512, <https://arxiv.org/abs/1107.0150>
- [53] A. Bakry, M. Deliyergiyev, A. Galal, M. Khalil, A. G. Williams, *On QCD strings beyond non-interacting model*, [arXiv:hep-lat/2001.04203]
- [54] O. Borisenko, V. Chelnokov, E. Mendicelli, A. Papa, *Three-quark potentials in an SU(3) effective Polyakov loop model*, Nucl. Phys. **B940** (2019), 214-238 [arXiv:1812.05384 [hep-lat]].
- [55] E. Megías, E. Ruiz Arriola, L. L. Salcedo, *Baryonic susceptibilities, quark-diquark models and quark-hadron duality at finite temperature*, Phys. Rev. **D99** (2019) no.7, 074020 [arXiv:1812.09365 [hep-ph]].
- [56] X. Chen, B. Yu, P. C. Chu and X. h. Li, *Studying the potential of QQq at finite temperature in a holographic model \**, Chin. Phys. C **46** (2022) no.7, 073102 [arXiv:2112.06234 [hep-ph]].
- [57] G. Parisi, *Quark Imprisonment and Vacuum Repulsion*, Phys.Rev. **D11** (1975) 970.
- [58] S. Mandelstam, *Vortices and Quark Confinement in Nonabelian Gauge Theories*, Phys. Rept. **23** (1976) 245–249.

- [59] M. Lüscher, K. Symanzik, P. Weisz, *Anomalies of the free loop wave equation in the WKB approximation*, Nucl. Phys. **B173** (1980) 365.
- [60] M. Creutz (1980) *Monte Carlo study of quantized SU(2) gauge theory*. Phys. Rev. **D21**:2308–2315.
- [61] M. Creutz, L. Jacobs, C. Rebbi, *Monte Carlo computations in lattice gauge theories*. Phys. Rept.**95** (1983) 201.
- [62] Creutz M (1981) *Monte Carlo study of renormalization in lattice gauge theory*. Phys. Rev. **D23**:1815.
- [63] Creutz M (1980) *Quark confinement*. Madison H.E. Physics **296**.
- [64] M. Fukugita, T. Niuya (1983), *Distribution of Chromoelectric Flux in SU(2) Lattice Gauge Theory*. Phys. Lett. **B132**, 374.
- [65] J. W. Flower, S. W. Otto (1985), *The Field Distribution in SU(3) Lattice Gauge Theory*. Phys. Lett. **B160**, 128 .
- [66] J. Wosiek, R. W. Haymaker (1987), *On the Space Structure of Confining Strings*. Phys. Rev. **D36**, 3297.
- [67] R. Sommer (1987), *Chromoflux Distribution in Lattice QCD*. Nucl. Phys. **B 291**, 673.
- [68] A. Di Giacomo, M. Maggiore, S. Olejnik (1990), *Evidence for Flux Tubes From Cooled QCD Configurations*. Phys. Lett. **B 236**, 199.
- [69] A. Di Giacomo, M. Maggiore, S. Olejnik (1990), *Confinement and Chromoelectric Flux Tubes in Lattice QCD*. Nucl. Phys. **B 347**, 441.
- [70] R. W. Haymaker, V. Singh, Y. C. Peng, J. Wosiek (1996), *Distribution of the color fields around static quarks: Flux tube profiles*. Phys. Rev. **D53**, 389 [hep-lat/9406021].
- [71] P. Cea, L. Cosmai (1995), *Dual superconductivity in the SU(2) pure gauge vacuum: A Lattice study*. Phys. Rev. **D52**, 5152 [hep-lat/9504008].
- [72] F. Okiharu, R. M. Woloshyn (2004), *A Study of color field distributions in the baryon*. Nucl. Phys. Proc. Suppl. **129**, 745 [hep-lat/0310007].
- [73] G.S. Bali, K. Schilling, C. Schlichter, *Observing long color flux tubes in SU(2) lattice gauge theory*, Phys. Rev. **D51** (1995) 5165–5198, <https://arxiv.org/abs/hep-lat/9409005>
- [74] E.V. Thuneberg, *Ginzburg-Landau theory of vortices in superfluid  $^3\text{He-B}$* , Phys. Rev. **B36** (1987) 3583–3597.
- [75] M.G. Alford, G. Good, *Flux tubes and the type-i/type-ii transition in a superconductor coupled to a superfluid*, Phys. Rev. **B78** (2008) 024510.

- [76] K. Kasamatsu, M. Tsubota, *Quantized vortices in atomic Bose-Einstein condensates*, (2007). Prog. Low Temp.Phys. **16** (2008) 351–403, <http://arxiv.org/abs/0709.1042>.
- [77] H.B. Nielsen, P. Olesen, *Vortex-line models for dual strings*, Nucl.Phys. **B61** (1973) 45 – 61.
- [78] A.S. Lo, E.L. Wright, *Signatures of cosmic strings in the cosmic microwave background*, <http://arxiv.org/abs/astro-ph/0503120>.
- [79] A. Patrascioiu, *Quantum Dynamics of a Massless Relativistic String. 2*, Nucl. Phys. **B81**, 525-546 (1974)
- [80] W.A. Bardeen, I. Bars, A.J. Hanson, R.D. Peccei, *A Study of the Longitudinal Kink Modes of the String*, Phys. Rev. **D13**, 2364-2382 (1976)
- [81] I. Bars, *Exact Equivalence of Chromodynamics to a String Theory*, Phys. Rev. Lett. **36**, 1521 (1976)
- [82] B. Brandt, and M. Meineri, *Effective string description of confining flux tubes*, Int. J. Mod. Phys. A, **31**, 1643001 (2016). [arXiv:hep-th/1603.06969].
- [83] S. Dubovsky, R. Flauger, V. Gorbenko, *Effective String Theory Revisited*, JHEP **09**, 044 (2012), [arXiv:hep-th/1203.1054].
- [84] N Brambilla, M. Groher, H. E. Martinez, A. Vairo, *Effective string theory and the long-range relativistic corrections to the quark-antiquark potential*, Phys. Rev. **D90**, 114032 (2014) no.11, [arXiv:hep-th/1407.7761].
- [85] K. Akemi *et al.* [QCD-TARO], *Autocorrelation in Updating Pure SU(3) Lattice Gauge Theory by the use of Overrelaxed Algorithms*, Nucl. Phys. B Proc. Suppl. **30** (1993), 253-256,
- [86] J. Polchinski, A. Strominger, *Effective string theory*, Phys. Rev. Lett. **67** (1991) 1681–1684.
- [87] M. Caselle, F. Gliozzi, U. Magnea, S. Vinti, *Width of long colour flux tubes in lattice gauge systems*, Nucl. Phys. **B460** (1996) 397–412, <http://arxiv.org/abs/hep-lat/9510019>
- [88] M. Lüscher, P. Weisz, *Quark confinement and the bosonic string*, JHEP **07** (2002) 049, <http://arxiv.org/abs/hep-lat/0207003>.
- [89] K.J. Juge, J. Kuti, C. Morningstar, *Fine structure of the QCD string spectrum*, Phys. Rev. Lett. **90** (2003) 161601, <http://arxiv.org/abs/hep-lat/0207004>.
- [90] M. Lüscher, G. Münster, P. Weisz, *How thick are chromoelectric flux tubes?*, Nucl. Phys. **B180** (1981) 1–12.

- [91] M. Caselle, M. Pepe, A. Rago, *Static quark potential and effective string corrections in the (2+1)-d SU(2) Yang-Mills theory*, JHEP **10** (2004) 005, <http://arxiv.org/abs/hep-lat/0406008>.
- [92] J. Kogut, L. Susskind, *Hamiltonian Formulation of Wilson's Lattice Gauge Theories*, Phys. Rev. **D11** (1975), 395–408
- [93] S. Capstick, N. Isgur, *Baryons in a relativized quark model with chromodynamics*, Phys. Rev. **D34(9)** (1986), 2809-2835
- [94] N. Brambilla, G.M. Prospero, A. Vairo, *Three body relativistic flux tube model from QCD Wilson loop approach*, Phys. Lett. **B362** (1995) 113–122, <https://arxiv.org/abs/hep-ph/9507300>
- [95] N. Brambilla, G. M. Prospero, A. Vairo, *Symmetries of the three-heavy-quark system and the color-singlet static energy at next-to-next-to-leading logarithmic order*, Phys. Rev. **D87**, 074014 (2013) [arXiv:hep-ph/1301.3013]
- [96] N. Brambilla, G. Ghiglieri, A. Vairo, *The Three-quark static potential in perturbation theory*, Phys. Rev. **D81**, 054031 (2010) [arXiv:hep-ph/0911.3541]
- [97] A. Bazavov *et al.* [TUMQCD Collaboration], *Determination of the QCD coupling from the static energy and the free energy*, Phys.Rev. **D100** (2019) no.11, 114511, [arXiv:1907.11747].
- [98] A. Allais, M. Caselle, *On the linear increase of the flux tube thickness near the deconfinement transition*, JHEP **01** (2009) 073. <http://arxiv.org/abs/0812.0284>
- [99] F. Gliozzi, M. Pepe, UJ. Wiese, *The Width of the Confining String in Yang-Mills Theory*. Phys. Rev. Lett. **104** (2010) 232001.
- [100] F. Gliozzi, M. Pepe, UJ. Wiese, *The Width of the Color Flux Tube at 2-Loop Order*. JHEP **11** (2010), 053.
- [101] K. Dietz, T. Filk, *Renormalization of string functionals*. Phys. Rev. **D27** (1983) 2944–2955,
- [102] O. Aharony, M. Field, *On the effective theory of long open strings*. JHEP **01** (2011), 065.
- [103] M. Billo, M. Caselle, F. Gliozzi, M. Meineri, R. Pellegrini, *The Lorentz-invariant boundary action of the confining string and its universal contribution to the interquark potential*. JHEP **05** (2012), 130.
- [104] M. Caselle, M. Hasenbusch, M. Panero, *Comparing the Nambu-Goto string with LGT results*. JHEP **03** (2005), 026.
- [105] M. Caselle *et al.* *Rough interfaces beyond the Gaussian approximation*. Nucl. Phys. B432:590–620 (1994).

- [106] M. Caselle, M. Hasenbusch, M. Panero, *Short distance behavior of the effective string*. JHEP **05** (2004), 032.
- [107] A. Athenodorou, B. Bringoltz, M. Teper, *Closed flux tubes and their string description in  $D=3+1$   $SU(N)$  gauge theories*. JHEP **02** (2011), 030 .
- [108] A. Athenodorou, B. Bringoltz, M. Teper, *Closed flux tubes and their string description in  $D=2+1$   $SU(N)$  gauge theories*. JHEP **05** (2011), 042.
- [109] J. Ambjorn, Y. Makeenko, A. Sedrakyan, *Effective QCD string beyond the Nambu-Goto action*. Phys. Rev. **D89(10)**, 106010 (2014).
- [110] T. Kalaydzhyan, E. Shuryak, *Self-interacting QCD strings and string balls*. Phys. Rev. **D90(2)**, 025031 (2014).
- [111] M. Caselle, M. Panero, R. Pellegrini, D. Vadicchino, *A different kind of string*. JHEP **01** (2015), 105.
- [112] B.B. Brandt, *Spectrum of the open QCD flux tube and its effective string description I: 3d static potential in  $SU(N = 2,3)$* . JHEP **07** (2017), 008.
- [113] M. Caselle, M. Hasenbusch, M. Panero *High precision Monte Carlo simulations of interfaces in the three-dimensional ising model: A Comparison with the Nambu-Goto effective string model*. JHEP **03** (2006), 084. arXiv[hep-lat/0601023]
- [114] S. Dubovsky, R. Flauger, V. Gorbenko, *Evidence from Lattice Data for a New Particle on the Worldsheet of the QCD Flux Tube*, Phys. Rev. Lett. **111**, 062006 (2013), [arXiv:hep-th/1301.2325].
- [115] N. Battelli, C. Bonati, *Color flux tubes in  $SU(3)$  Yang-Mills theory: an investigation with the connected correlator*, Phys. Rev. **D99** (2019), no.11, 114501 [arXiv:1903.10463 [hep-lat]].
- [116] P. Cea, L. Cosmai, F. Cuteri, A. Papa, *Flux tubes in the QCD vacuum*, Phys. Rev. **D95** (2017) no.11, 114511 [arXiv:1702.06437 [hep-lat]].
- [117] C. Bonati, M. Caselle, S. Morlacchi, *The Unreasonable effectiveness of effective string theory: The case of the 3D  $SU(2)$  Higgs model*, Phys. Rev. **D104** (2021) no.5, 054501 [arXiv:2106.08784 [hep-lat]].
- [118] M. Caselle, *Effective String Description of the Confining Flux Tube at Finite Temperature*, Universe **7** (2021) no.6, 170 [arXiv:2104.10486 [hep-lat]].
- [119] B. B. Brandt, *Revisiting the flux tube spectrum of 3d  $SU(2)$  lattice gauge theory*, Indian J. Phys. **95** (2021) no.8, 1613-1622 [arXiv:2102.06413 [hep-lat]].
- [120] M. N. Khalil, A. M. Khalaf, A. Bakry, M. Deliyergiyev, A. Galal, M. Koteb, M. D. Okasha and S. Ahmed, *Unveiling bosonic string effects in Wilson loops via boundary action in  $SU(2)$  Yang-Mills theory*, [arXiv:2210.04586 [hep-th]].

- [121] M. Caselle, M. Panero, D. Vadicchino, *Squared width and profile of the confining flux tube in the  $U(1)$  LGT in 3D*, PoS **LATTICE2016** (2017), 347 [arXiv:1610.08315 [hep-lat]].
- [122] M. Caselle, M. Panero, D. Vadicchino, *Width of the flux tube in compact  $U(1)$  gauge theory in three dimensions*, JHEP **02** (2016), 180 [arXiv:1601.07455 [hep-lat]].
- [123] A.S. Bakry, D.B. Leinweber, B. Derek, A. G. Williams, *The Thermal Delocalization of the Flux Tubes in Mesons and Baryons*, AIP Conference Proceedings **1354** (2011) 178-183, <https://aip.scitation.org/doi/pdf/10.1063/1.3587603>
- [124] P. Giudice, F. Gliozzi, S. Lottini, *The Confining string beyond the free-string approximation in the gauge dual of percolation*, JHEP **03** (2009) 104, <http://arxiv.org/abs/0901.0748>
- [125] M. Lüscher, P. Weisz, *String excitation energies in  $SU(N)$  gauge theories beyond the free-string approximation*, JHEP **07** (2004) 014.
- [126] O. Kaczmarek, F. Karsch, E. Laermann, M. Lutgemeier, *Heavy quark potentials in quenched QCD at high temperature*, Phys. Rev. **D62**, 034021 (2000)
- [127] N. Cardoso and P. Bicudo, *Lattice QCD computation of the  $SU(3)$  string tension critical curve*, Phys. Rev. **D85**, 077501 (2012)
- [128] O. Andreev, *Some multi-quark potentials, pseudo-potentials and AdS/QCD*, Phys. Rev. **D78**, 065007 (2008), [arXiv:hep-ph/0804.4756].
- [129] O. Andreev, *Drag force on heavy diquarks and gauge/string duality*, Phys. Rev. **D98**, 066007 (2018) no.6.
- [130] J. Flower, *Baryons on the lattice.1. Rotational Symmetry*, Nucl. Phys. **B 289**, 484 (1987).
- [131] T. T. Takahashi, H. Matsufuru, Y. Nemoto, H. Suganuma, Phys. Rev. Lett. **86**, 18 (2001);  
T. T. Takahashi, H. Suganuma, Y. Nemoto, H. Matsufuru, *Detailed analysis of the three quark potential in  $SU(3)$  lattice QCD*, Phys. Rev. **D65**, 114509 (2002) [arXiv:hep-lat/0204011].
- [132] H. Ichie, V. Bornyakov, T. Streuer, G. Schierholz, *The flux distribution of the three quark system in  $SU(3)$* , Nucl. Phys. Proc. Suppl. **119**, 751 (2003) [arXiv:hep-lat/0212024].  
V. G. Bornyakov *et al.* [DIK Collaboration], *Baryonic flux in quenched and two-flavor dynamical QCD*, Phys. Rev. **D70**, 054506 (2004) [arXiv:hep-lat/0401026].
- [133] F. Bissey *et al.*, *Gluon flux-tube distribution and linear confinement in baryons*, Phys. Rev. **D76** (2007) 114512, <https://arxiv.org/abs/hep-lat/0606016>.

- [134] J. M. Cornwall, *On the centre-vortex baryonic area law*, Phys. Rev. **D69**, 065013 (2004) [arXiv:hep-th/0305101].
- [135] F. J. Llanes-Estrada, O. I. Pavlova, R. Williams, *A First Estimate of Triply Heavy Baryon Masses from the pNRQCD Perturbative Static Potential*, Eur. Phys. J. **C72** (2012), 2019 [arXiv:1111.7087 [hep-ph]].
- [136] G. 't Hooft, High Energy Physics, EPS International Conference, Palermo (1975).
- [137] S. M. Christensen, *Vacuum expectation value of the stress tensor in an arbitrary curved background: The covariant point-separation method*, Phys. Rev. **D14**, 2490–2501 (1976) 10.1103/PhysRevD.14.2490
- [138] S. M. Christensen, *Regularization, renormalization, and covariant geodesic point separation*, Phys. Rev. **D17**, 946–963 (1978) 10.1103/PhysRevD.17.946
- [139] M. Caselle, *Flux tube delocalization at the deconfinement point*, JHEP **08** (2010) 063. <http://arxiv.org/abs/1004.3875>
- [140] C. Bonati, *Finite temperature effective string corrections in (3+1)D SU(2) lattice gauge theory*, Phys.Lett. **B703** (2011) 376–378, <http://arxiv.org/abs/1106.5920>
- [141] F. Gliozzi, *Quantum behavior of the flux tube: A Comparison between QFT predictions and lattice gauge theory simulations. International Conference on Quark Confinement and the Hadron Spectrum* (1994) <https://arxiv.org/abs/hep-lat/9410022>
- [142] Y. Koma, M. Koma, *Precise determination of the three-quark potential in SU(3) lattice gauge theory*, Phys. Rev. **D95** (9) (2017) 094513, <http://arxiv.org/abs/1703.06247>.
- [143] F. Bissey, A.I. Signal, D.B. Leinweber, *Comparison of gluon flux-tube distributions for quark-diquark and quark-antiquark hadrons*, Phys. Rev. **D80**, 114507 (2009), [arXiv:hep-lat/0910.0958].
- [144] R.S. Kaushal, D.S. Kulshreshtha, *Quark Confinement Potential and the Quark-Diquark Model for Nucleons*, Annals Phys. **108**, 198-211 (1977)
- [145] A. Bazavov *et al.* [TUMQCD Collaboration], *Color screening in (2+1)-flavor QCD*, Phys. Rev. **D98** (2018) no.5, 054511 [arXiv:hep-lat/1804.10600].
- [146] T.T. Takahashi, H. Matsufuru, Y. Nemoto, H. Suganuma, *The Three quark potential in the SU(3) lattice QCD*, Phys. Rev. Lett. **86** (2001), 18–21, <https://arxiv.org/abs/hep-lat/0006005>
- [147] C. Gattringer, C. B. Lang, *Quantum Chromodynamics on the Lattice*, Lect. Notes Phys. **788**, 1 (2010).
- [148] N. Cardoso, M. Cardoso, P. Bicudo, *Inside the SU(3) quark-antiquark QCD flux tube: screening versus quantum widening*, Phys. Rev **D88**,(2013) 054504.

- [149] K.G. Wilson, *Confinement of quarks*, Phys. Rev. **D10** (1974) no.8, 2445
- [150] R. Sommer, *A New way to set the energy scale in lattice gauge theories and its applications to the static force and alpha-s in SU(2) Yang-Mills theory*, Nucl. Phys. **B411**, 839-854 (1994) [arXiv:hep-lat/9310022].
- [151] M. Lüscher, P. Weisz, *On-Shell Improved Lattice Gauge Theories*, Commun. Math. Phys. **97**, 59 (1985) [Erratum-ibid. **98**, 433 (1985)].
- [152] K. Fabricius, O. Haan, *Heat Bath Method for the Twisted Eguchi-Kawai Model*, Phys. Lett. **B 143**, p.459-462 (1984).
- [153] A.D. Kennedy, B.J. Pendleton, *Improved Heat Bath Method for Monte Carlo Calculations in Lattice Gauge Theories*, Phys. Lett. **B 156**, p.393-399 (1985).
- [154] N. Cabibbo, E. Marinari, *A New Method for Updating SU(N) Matrices in Computer Simulations of Gauge Theories*, Phys. Lett. **B 119**, 387-390 (1982).
- [155] F. Bissey *et al.* *Gluon field distribution in baryons*, Nucl. Phys. B Proc. Suppl. **141** (2005) 22–25, <https://arxiv.org/abs/hep-lat/0501004>.
- [156] M. Lüscher, P. Weisz, *Locality and exponential error reduction in numerical lattice gauge theory*, JHEP **09** (2001), 010, <https://arxiv.org/abs/hep-lat/0108014>.
- [157] M. Feurstein, H. Markum, and S. Thurner, *QCD phase transitions. Proceedings, 25th International Workshop on Gross Properties of Nuclei and Nuclear Excitations, Hirschegg, Austria, January 13-18, 1997*, Phys. Rev. **D88** (2013) 054504, <http://arxiv.org/abs/9702006>.
- [158] S. Thurner *et al.* *Topological and Chiral Structure in Lattice QCD at Finite Temperature, International Europhysics Conference on HEP, 19–25 August 1997*, pp.1023–1027, (1999).
- [159] C. Morningstar, M.J. Peardon, *Analytic smearing of SU(3) link variables in lattice QCD*, Phys. Rev. **D69**, 054501 (2004), [arXiv:hep-lat/0311018].
- [160] F.D.R. Bonnet, D.B. Leinweber, A.G. Williams, J.M. Zanotti, *Improved smoothing algorithms for lattice gauge theory*, Phys. Rev. **D65**, 114510 (2002). [arXiv:hep-lat/0106023].
- [161] M. Albanese *et al.* [APE Collaboration], *Glueball Masses And String Tension In Lattice QCD*, Phys. Lett. **B 192**, 163 (1987).
- [162] P. Weisz, *Renormalization and lattice artifacts*, Les Houches Summer School 2009, <https://arxiv.org/abs/1004.3462>.
- [163] C. Alexandrou, P. De Forcrand, A. Tsapalis, *The static three-quark SU(3) and four-quark SU(4) potentials*, Phys. Rev. **D65**, 054503 (2002) [arXiv:hep-lat/0107006].

- [164] C. Alexandrou, P. de Forcrand, O. Jahn, *The ground state of three quarks*, Nucl. Phys. Proc. Suppl. **119**, 667 (2003) [arXiv:hep-lat/0209062].
- [165] H. Kleinert, *Exact Temperature Behavior of Strings With Extrinsic Curvature Stiffness for  $D \rightarrow \infty$ : Thermal Deconfinement Transition*, Phys. Rev. **D40**, (1989) 473–490.
- [166] K. S. Viswanathan, Xiao-An Zhou, *Free energy and the static potential for open smooth strings*. Int. J. Mod. Phys. **A3** (1988), 2195–2206.
- [167] N. Cardoso, M. Cardoso, P. Bicudo, *Inside the  $SU(3)$  quark-antiquark QCD flux tube: screening versus quantum widening*, Phys. Rev. **D88** (2013) 054504, <http://arxiv.org/abs/1302.3633>.
- [168] T. Takahashi, H. Suganuma, *Detailed Analysis of Gluonic Excitation in Three-Quark Systems in Lattice QCD*, Phys. Rev. **D70**, 074506 (2004).
- [169] P. Bicudo, M. Cardoso, N. Cardoso *Colour fields of the quark-antiquark excited flux tube*, Proceedings, 35th International Symposium on Lattice Field Theory (Lattice 2017): Granada, Spain, June 18-24, 2017, EPJ Web Conf., **175**, 14009 (2018). [arXiv:hep-lat/1803.04569].
- [170] G. S. Bali, F. Bruckmann, G. Endrodi, Z. Fodor, S. D. Katz, A. Schafer, *QCD quark condensate in external magnetic fields*, Phys. Rev. **D86**, 071502 (2012), [arXiv:hep-lat/1206.4205].
- [171] M. N. Chernodub, *QCD string breaking in strong magnetic field*, Modern Physics Letters A, **29**, 1450162 (2014).
- [172] C. Bonati, S. Cali, M. D’Elia, M. Mesiti, F. Negro, A. Rucci, F. Sanfilippo, *Effects of a strong magnetic field on the QCD flux tube*, Phys. Rev. **D98** (2018) no.5, 054501 [arXiv:1807.01673 [hep-lat]].
- [173] C. Bonati, S. Salvatore, M. D’Elia, M. Mesiti, F. Negro, A. Rucci, F. Sanfilippo, *Flux tubes in  $N_f = 2 + 1$  QCD with external magnetic fields*, EPJ Web Conf. **175**, 12008 (2018).
- [174] A. D. Marques Valois, B. Brandt, F. Cuteri, G. Endrodi, G. Marko, *“Lattice QCD with an inhomogeneous magnetic field background*, PoS **LATTICE2021** (2022), 083 [arXiv:2111.13100 [hep-lat]].